CrossMark

The Hubble Constant from Strongly Lensed Supernovae with Standardizable Magnifications

Simon Birrer[1,2] , Suhail Dhawan[3] , and Anowar J. Shajib[4]

[1] Kavli Institute for Particle Astrophysics and Cosmology and Department of Physics, Stanford University, Stanford, CA 94305, USA; sibirrer@stanford.edu
[2] SLAC National Accelerator Laboratory, Menlo Park, CA 94025, USA
[3] Kavli Institute of Cosmology/Institute of Astronomy, University of Cambridge, Madingley Road, Cambridge CB3 0HA, UK
[4] Department of Astronomy & Astrophysics, University of Chicago, Chicago, IL 60637, USA

Abstract

The dominant uncertainty in the current measurement of the Hubble constant (H_0) with strong gravitational lensing time delays is attributed to uncertainties in the mass profiles of the main deflector galaxies. Strongly lensed supernovae (glSNe) can provide, in addition to measurable time delays, lensing magnification constraints when knowledge about the unlensed apparent brightness of the explosion is imposed. We present a hierarchical Bayesian framework to combine a data set of SNe that are not strongly lensed and a data set of strongly lensed SNe with measured time delays. We jointly constrain (i) H_0 using the time delays as an absolute distance indicator, (ii) the lens model profiles using the magnification ratio of lensed and unlensed fluxes on the population level, and (iii) the unlensed apparent magnitude distribution of the SN population and the redshift–luminosity relation of the relative expansion history of the universe. We apply our joint inference framework on a future expected data set of glSNe and forecast that a sample of 144 glSNe of Type Ia with well-measured time series and imaging data will measure H_0 to 1.5%. We discuss strategies to mitigate systematics associated with using absolute flux measurements of glSNe to constrain the mass density profiles. Using the magnification of SN images is a promising and complementary alternative to using stellar kinematics. Future surveys, such as the Rubin and Roman observatories, will be able to discover the necessary number of glSNe, and with additional follow-up observations, this methodology will provide precise constraints on mass profiles and H_0.

1. Introduction

The current expansion rate of the universe, the Hubble constant H_0, anchors the scale and the age of the universe. There is an ongoing debate about the precise value of H_0, where some local distance ladder measurements based on calibration using Cepheids (e.g., Riess et al. 2021) are in significant statistical disagreement with measurements extrapolated from the cosmic microwave background (CMB; e.g., Aiola et al. 2020; Planck Collaboration et al. 2020). Another distance ladder analysis based on calibration using the tip of the red giant branch (TRGB) stars results in a consistent measurement with the CMB (Freedman et al. 2020; Freedman 2021). This discrepancy indicates either unaccounted-for systematics in one or multiple measurements (e.g., Efstathiou 2020; Mortsell et al. 2021) or new physics beyond the standard model of cosmology. Multiple independent and precise measurements of H_0 are essential in providing a definite resolution to the current tension.

Relative time delays between multiple gravitationally lensed images provide a one-step distance anchor of the universe, and thus H_0. This probe is independent of the local distance ladder and the sound-horizon-physics anchors of the CMB and large-scale structure probes. The method, known as the time-delay cosmography, has been proposed more than half a century ago to utilize the transient nature of supernovae (SNe) for

measuring the time delays (Refsdal 1964). Time-delay cosmography was first applied by measuring the time delays of multiply lensed quasars with multiseason monitoring campaigns (e.g., Kundić et al. 1997; Schechter et al. 1997; Fassnacht et al. 2002; Tewes et al. 2013; Courbin et al. 2018; Millon et al. 2020a). The discovery of numerous lensed quasar systems, follow-up monitoring, high-resolution imaging, and precise spectroscopic observations have led to a precise measurement of H_0 using seven multiply lensed quasars (Wong et al. 2020; Shajib et al. 2020; Millon et al. 2020b). These measurements assumed particular forms of the mass density profiles of the deflector galaxies. The mass-sheet degeneracy (MSD; see Falco et al. 1985; Schneider & Sluse 2013), an inherent transform leaving the lensing observables invariant while changing the time-delay prediction, poses limits in the precision of H_0 measurements in the absence of additional data. Birrer et al. (2020) introduced an additional degree of freedom to the mass density profiles to avoid constraining the lens model based on the specific form of the mass profiles previously chosen. Birrer et al. (2020) constrained the MSD solely by stellar kinematics observations of the deflector galaxy hierarchically on the deflector population-level mitigating covariances among the assumptions of individual lenses. For the achieved 5% precision measurement of H_0, Birrer et al. (2020) combined the seven TDCOSMO lenses with 33 galaxy–galaxy lenses from the Sloan Lens ACS (SLACS) survey (Bolton et al. 2008; Shajib et al. 2021). The interpretation of the kinematics measurements is impacted by the mass-anisotropy degeneracy (Binney & Mamon 1982; Dejonghe & Merritt 1992), and mitigating this degeneracy requires assumption

on the stellar anisotropy distribution or spatially resolved kinematics measurements (e.g., Cappellari 2008; Barnabè et al. 2011; Yıldırım et al. 2020). A forecast for future constraints using kinematics observations in breaking the MSD within the assumptions of the Birrer et al. (2020) analysis is provided by Birrer & Treu (2021).

An alternative to lensed quasars, as in fact anticipated in the original work by Refsdal (1964), are multiply resolved gravitationally lensed SNe (glSNe). glSNe are exquisite laboratories for fundamental physics, as well as astrophysical properties of the host and lens galaxies (see Oguri 2019, for a review of strong lensing of SNe and other explosive transients). We refer to Goobar et al. (2002), for example, for early explorations of cosmological parameter forecasts with hundreds of glSNe.

Although strongly lensed galaxies and quasars (QSOs) are more common than currently discovered occurrences of glSNe, glSNe have notable advantages, particularly if they are of Type Ia (SNe Ia). The luminosities of SNe Ia have a small dispersion after correcting for the relations with the light-curve shape, observed color, and properties of their host galaxies, making them a "standardizable candle" (see, e.g., Phillips 1993; Guy et al. 2007; Scolnic et al. 2018). Knowledge about the apparent magnitude, at the source redshift of the SNe, in the absence of any lensing effect allows us to directly measure the lensing magnification factor at the locations relevant to predict the time delays, breaking the MSD (see also, e.g., Kolatt & Bartelmann 1998; Oguri & Kawano 2003; Foxley-Marrable et al. 2018). Thus, breaking the MSD does not require an a priori knowledge of the SN Ia absolute magnitude, thus keeping the inference from time-delay cosmography independent from the local distance ladder calibration. Additionally, SNe Ia have a well-studied family of light curves with a well-defined maximum at ~18 days from explosion (e.g., Yao et al. 2019; Miller et al. 2020) and hence can be used for an accurate measurement of time delays, with significantly fewer follow-up observations than quasars. Recent simulations of lensed SNe Ia also find that the time-delay measurement is not impacted significantly from microlensing (Goldstein et al. 2018; Huber et al. 2021). Moreover, since SNe fade away, we can obtain post-explosion imaging to validate the lens model (see, e.g., Ding et al. 2021).

glSNe Ia are also complementary to lensed QSOs in the strategy for discovering these systems. Owing to their small luminosity scatter, glSNe Ia can be discovered owing to the lensing magnification increasing their brightness. This would not need highly spatially resolved observations, as is the case for lensed QSOs, important for testing potential biases from selecting high angular separation events. This was demonstrated in the discovery of the first resolved strongly lensed SN Ia, iPTF16geu (Goobar et al. 2017). At $z = 0.409$, the SN was found to be 30 standard deviations too bright compared with the SN Ia population, prompting space-based and laser-guided star–adaptive optics (LGS-AO) follow-up. While iPTF16geu had a short time delay of ~1 day (Goobar et al. 2017; More et al. 2017), hence not ideal for measuring H_0, the system could uniquely be used for a direct inference of the lensing magnification (e.g., Foxley-Marrable et al. 2018; Dhawan et al. 2020). Simulations of wide-field surveys like the Zwicky Transient Factory (ZTF) suggest a median time delay of ~1–5 days (Goldstein et al. 2019; Wojtak et al. 2019) based on a magnification discovery channel. Upcoming deeper

surveys, such as the Vera Rubin Observatory Legacy Survey of Space and Time (LSST), are expected to discover glSNe based on image multiplicity at fainter magnitudes, shifting the median time delay to ~10 days (Wojtak et al. 2019), making glSNe Ia compelling probes of H_0. glSNe also offer a unique opportunity to obtain time delays from resolved spectroscopy, a method that requires very few epochs of observations (Johansson et al. 2021; Bayer et al. 2021).

With the advent of transient astrophysics and the anticipated discovery of more glSNe from current and future time-domain facilities, glSNe can play a major and complementary role in time-delay cosmography and beyond. In particular, the complementarity in constraining the MSD with magnification measurements in addition to stellar kinematics measurements allows one to rigorously check for systematics inherent in either of the two approaches, as well as gain further statistical precision in the most limiting domain of time-delay cosmography to date.

Additionally, strong gravitational lensing systems are powerful probes of elliptical galaxy properties and evolution (e.g., Treu & Koopmans 2002; Auger et al. 2010; Shajib et al. 2021). Nonimaging data—such as the time delays, the stellar kinematics, or the image magnifications—provide additional constraints on the gravitational potential, or equivalently the mass distribution. In such studies, the adopted values of cosmological parameters can indeed have significant physical outcomes. For example, Blum et al. (2020) demonstrated that adopting the CMB-based H_0 value for the seven TDCOSMO systems leads to galaxy mass distributions with a cored component in the dark matter profile. However, Shajib et al. (2021) combined only the stellar kinematics with the lens imaging data (without any time-delay measurement) to find that the deviation from the power-law profile in elliptical galaxies can also be caused by a higher normalization in the dark matter profile instead of having a cored component. The hierarchical analysis of Birrer et al. (2020) simultaneously constrained both the mass distribution in galaxies and H_0 for the first time from the combination of stellar kinematics and lensing information. glSNe Ia will similarly provide simultaneous constraints on the galaxy mass distribution and cosmological parameters. Furthermore, a sufficiently large glSN Ia sample spanning a wide redshift range can provide direct insights into the evolution of massive elliptical galaxies.

In this paper, we aim to exploit the uniform behavior of the population of SNe Ia to reduce uncertainties in the lens modeling arising from the MSD. We extend the hierarchical inference framework by Birrer et al. (2020) and incorporate SN Ia apparent magnitudes, for both lensed and global unlensed populations, on the likelihood level in the cosmographic inferences. We perform forecasts at the same level of complexity as presented by Birrer & Treu (2021), now replacing the kinematics observables with SN Ia brightness measurements, for different scenarios and highlight the key ingredients required to achieve an H_0 measurement with precision below 2%.

The paper is structured as follows. Section 2 provides a general review on the key concepts of time-delay cosmography, with a special focus on the MSD and approaches to constrain it. Section 3 defines the methodology, model parameterization, likelihood, and sampling approach used for the forecasts. Section 4 presents different forecast scenarios with regard to H_0 inferences. We discuss the key components

and implications of this work in Section 5 and conclude in Section 6.

The formalism and inference schemes presented in this work are implemented in the open-source software HIERARC,[5] and the scripts to reproduce the presented work are publicly available.[6] Lensing calculations are performed with LENSTRONOMY[7] (Birrer & Amara 2018; Birrer et al. 2021).

2. Time-delay Cosmography with Strongly Lensed SNe

In this section, we review the principles of time-delay cosmography for lensing and time delays (Section 2.1). We then emphasize how an MSD affects the observables and thus the inference of cosmographic quantities, and we specifically discuss the ability of glSNe in breaking the MSD with absolute lensing magnifications (Section 2.2).

2.1. Cosmography with Strong Lenses

The phenomena of gravitational lensing can be described by the lens equation, which maps the source plane coordinate β to the image plane θ as

$$\beta = \theta - \alpha(\theta), \tag{1}$$

where α is the angular shift on the sky between the original unlensed position and the lensed observed position of an object.

For a single deflector plane, the lens equation can be expressed in terms of the physical deflection angle $\hat{\alpha}$ as

$$\beta = \theta - \frac{D_s}{D_{ds}}\hat{\alpha}(\theta), \tag{2}$$

where D_s and D_{ds} are the angular diameter distances from the observer to the source and from the deflector to the source, respectively. In the single lens plane regime, we can introduce the lensing potential ψ such that

$$\alpha(\theta) = \nabla\psi(\theta) \tag{3}$$

and the lensing convergence as

$$\kappa(\theta) = \frac{1}{2}\nabla^2\psi(\theta). \tag{4}$$

The relative arrival time Δt_{AB} between two images θ_A and θ_B originating from the same source is

$$\Delta t_{AB} = \frac{D_{\Delta t}}{c}[\tau(\theta_A, \beta) - \tau(\theta_B, \beta)] = \frac{D_{\Delta t}}{c}\Delta\tau_{AB}, \tag{5}$$

where c is the speed of light,

$$\tau(\theta, \beta) = \left[\frac{(\theta - \beta)^2}{2} - \psi(\theta)\right] \tag{6}$$

is the Fermat potential (Schneider 1985; Blandford & Narayan 1986), and

$$D_{\Delta t} \equiv (1 + z_d)\frac{D_d D_s}{D_{ds}} \tag{7}$$

is the time-delay distance (Refsdal 1964; Schneider et al. 1992; Suyu et al. 2010), with D_d the angular diameter distance from

the observer to the deflector. In the last line of Equation (5) we chose the notation $\Delta\tau_{AB}$ to describe the relative Fermat potential between two images.

Constraints on the Fermat potential difference $\Delta\tau_{AB}$ and a measured time delay Δt_{AB} allow us to constrain the time-delay distance $D_{\Delta t}$. This absolute physical distance anchors the scale in the universe within the redshifts involved in the lensing configuration. The Hubble constant is inversely proportional to the absolute scales of the universe and thus scales with $D_{\Delta t}$ as

$$H_0 \propto D_{\Delta t}^{-1}, \tag{8}$$

mildly dependent on the relative expansion history from current time ($z = 0$) to the redshifts of the deflector and the source.

2.2. The MST and the Ability of Lensing Magnifications in Breaking It

2.2.1. MST Impact on Time Delays and Imaging Data

The mass-sheet transform (MST) is a multiplicative transform of the lens equation (Equation (1)) given by

$$\lambda\beta = \theta - \lambda\alpha(\theta) - (1 - \lambda)\theta, \tag{9}$$

which preserves image positions (and any higher-order relative differentials of the lens equation) under a linear source displacement $\beta \to \lambda\beta$ (Falco et al. 1985). The term $(1 - \lambda)\theta$ in Equation (9) above describes an infinite sheet of convergence (or mass), hence the name MST. Only observables related to the unlensed apparent source size, to the unlensed apparent brightness, or to the lensing potential are able to break this degeneracy.

The convergence field transforms according to

$$\kappa_\lambda(\theta) = \lambda\kappa(\theta) + (1 - \lambda). \tag{10}$$

Thus, the same relative lensing observables can result if the mass profile is scaled by the factor λ with the addition of a sheet of convergence (or mass) of $\kappa(\theta) = (1 - \lambda)$.

The different observables described in Section 2.1 relevant for time-delay cosmography transform by an MST term λ as follows: the image positions remain invariant

$$\theta_\lambda = \theta; \tag{11}$$

the source position scales with λ as

$$\beta_\lambda = \lambda\beta; \tag{12}$$

the Fermat potential scales with λ as

$$\Delta\tau_{AB,\lambda} = \lambda\Delta\tau_{AB}, \tag{13}$$

and so does the time delay as

$$\Delta t_{AB,\lambda} = \lambda\Delta t_{AB}. \tag{14}$$

When transforming a deflector profile with an MST, the inference of the time-delay distance (Equation (7)) from a measured time delay and inferred Fermat potential transforms as

$$D_{\Delta t,\lambda} = \lambda^{-1}D_{\Delta t}. \tag{15}$$

Thus, the Hubble constant, when inferred from the time-delay distance $D_{\Delta t}$, transforms as (from Equation (8))

$$H_{0,\lambda} = \lambda H_0. \tag{16}$$

Achieving precise and accurate constraints on the radial density profile required to measure H_0 necessitates external data and puts high demand on the precision and accuracy of those measurements and priors. We refer the reader to Section 2 of Birrer et al. (2020) for a discussion on interpretations of an MST in regard to a parameterized profile and physical limits of it.

There are two promising observables that have the ability to break the MST independent of the time delays: the stellar velocity dispersion measurements of the deflector galaxy and the absolute magnification measurement from knowledge of the apparent unlensed brightness of a source component.

For the remainder of this paper, we chose the convention of λ to be the mapping from a model prediction ignoring MST effects to the target prediction of the correct answer.

2.2.2. Stellar Velocity Dispersion

The stellar velocity dispersion of the main deflector galaxy is directly sensitive to the deflector potential. Joint lensing and kinematics measurements have been used to constrain the mass profiles of massive elliptical galaxies (Shajib et al. 2021) and are the sole constraining anchor on the MST in the H_0 measurement by Birrer et al. (2020). The observed stellar velocity dispersion σ_v scales with an MST as

$$\sigma_{v,\lambda} = \sqrt{\lambda}\, \sigma_v. \qquad (17)$$

A fractional uncertainty in the velocity dispersion measurement $\sigma_{v,\,\mathrm{obs}}$ or model prediction $\sigma_{v,\,\mathrm{model}}$ propagates to a fractional uncertainty in the MST as

$$\frac{\delta\lambda}{\lambda} = 2\left[\frac{\delta\sigma_{v,\,\mathrm{obs}}}{\sigma_{v,\,\mathrm{obs}}} - \frac{\delta\sigma_{v,\,\mathrm{model}}}{\sigma_{v,\,\mathrm{model}}}\right], \qquad (18)$$

where we identified the target truth (measured) velocity dispersion with $\sigma_{v,\lambda} = \sigma_{v,\,\mathrm{obs}}$ and the model without the MST correction with $\sigma_v = \sigma_{v,\,\mathrm{model}}$ of Equation (17). Thus, an achievable 5% uncertainty in the measurement of σ_v propagates to a 10% uncertainty in λ. Beyond the measurement uncertainty in σ_v, projection uncertainties and degeneracies are present in the interpretation of the measurement, the model uncertainty. In particular, the mass-anisotropy degeneracy limits the precision, so only spatially resolved kinematics observations are able to break this secondary, but relevant, degeneracy (e.g., Yıldırım et al. 2020; Birrer & Treu 2021). Constraints on the radial extent of the mass profile with spatially resolved kinematics are possible. Equation (18) is, however, applicable for the covariant uncertainties among multiple measurements or integral field unit spectroscopy. A forecast utilizing kinematic measurements of ground- and space-based facilities on a larger sample of lenses within the same assumptions as Birrer et al. (2020) is presented by Birrer & Treu (2021).

2.2.3. Absolute Lensing Magnifications

An alternative to kinematics, and a key element in the exploration in this work, are absolute magnification constraints (Kolatt & Bartelmann 1998; Foxley-Marrable et al. 2018). Absolute lensing magnifications, μ, change under an MST by

$$\mu_\lambda = \lambda^{-2}\mu. \qquad (19)$$

A fractional uncertainty in the lensing magnification propagates to a fractional uncertainty in the MST as

$$\frac{\delta\lambda}{\lambda} = -0.5\frac{\delta\mu}{\mu} = -0.5\left[\frac{\delta\mu_{\mathrm{obs}}}{\mu_{\mathrm{obs}}} - \frac{\delta\mu_{\mathrm{model}}}{\mu_{\mathrm{model}}}\right]. \qquad (20)$$

The observed magnification μ_λ is the ratio

$$\mu_{\mathrm{obs}} = \frac{F_{\mathrm{obs}}}{F_{\mathrm{unl}}}, \qquad (21)$$

where F_{obs} is the observed flux of an image and F_{unl} is the unlensed apparent brightness of the object in the absence of the lensing effect. While measuring the observed flux of a lensed object is achieved to subpercent precision on a regular basis, a lensing-independent measurement of μ_λ requires, in addition, knowledge of the unlensed apparent brightness of the object in the same observational band as the measurement. We stress that the measurement of the lensing magnification does not require knowledge or calibration of the absolute luminosity, which is a key requirement in measuring H_0 with SNe Ia (e.g., Freedman et al. 2019; Riess et al. 2019). Only the probability distribution function of the apparent magnitude of the source at the redshift of the source is required.

The estimation of the MST scaling for a given lens model relevant for the time-delay prediction, and thus the measurement of H_0, requires, in addition, an accurate lensing magnification prediction in accordance with the Fermat potential prediction. While the time-delay prediction is less susceptible to small-scale model inaccuracies,[8] as it relies only on an accurate lensing potential, the local magnification is impacted more significantly, as it relies on the second-order differentials of the potential. In addition to small-scale dark matter structure, both along the line of sight (LOS) and within the main deflector as substructure, stellar microlensing is an additional source of lensing magnifications for sources of the size of exploding SNe (e.g., Dobler & Keeton 2006; Yahalomi et al. 2017; Foxley-Marrable et al. 2018; Suyu et al. 2020).

We can approximately separate the different components entering the local magnification prediction into a smooth macro-model component μ_{macro} and an additional perturbation by dark matter structure on milliarcsecond scales, $\Delta\mu_{\mathrm{milli}}$, and stellar microlensing, $\Delta\mu_{\mathrm{micro}}$, as[9]

$$\mu_{\mathrm{local}} \approx \mu_{\mathrm{macro}} + \Delta\mu_{\mathrm{milli}} + \Delta\mu_{\mathrm{micro}}. \qquad (22)$$

Millilensing depends on the halo substructure and on the LOS abundances of small field halos. Stellar microlensing depends on the local projected stellar surface density and can vary significantly from lens to lens and from image position to image position.

The relative difference in λ for either an infinitesimal change in the apparent unlensed magnitude, δF_{unl}, a change in the lensed observed flux, δF_{obs}, the model predicted magnification, $\delta\mu_{\mathrm{model}}$, or the physical cause of local millilensing (microlensing), $\delta\mu_{\mathrm{milli}}$ ($\delta\mu_{\mathrm{micro}}$), while keeping all other quantities fixed,

---

[8] See Gilman et al. (2020b) for the impact of unresolved small-scale dark matter structure on the predicted time delays, resulting in a scatter of about 2.5% on an individual lens; see also Liao et al. (2018) and Keeton & Moustakas (2009).
[9] Magnification effects are, in general, not additive. We justify the approximation by the different scales of macro-, milli-, and microlensing.

can be expressed as (Equations (20), (21), (22))

$$\frac{\delta\lambda}{\lambda} = 0.5 \left[\frac{\delta F_{\mathrm{unl}}}{F_{\mathrm{unl}}} - \frac{\delta F_{\mathrm{obs}}}{F_{\mathrm{obs}}} \right.$$
$$\left. + \frac{\delta\mu_{\mathrm{macro}}}{\mu} + \frac{\delta\Delta\mu_{\mathrm{milli}}}{\mu} + \frac{\delta\Delta\mu_{\mathrm{micro}}}{\mu} \right]. \qquad (23)$$

In words, while keeping all other parameters fixed, an increase in F_{unl} leads to an increase in λ, an increase in F_{obs} leads to a decrease in λ, and an increase in the lensing magnifications μ_{macro}, $\Delta\mu_{\mathrm{milli}}$, and $\Delta\mu_{\mathrm{milli}}$ leads to an increase in λ. On the other hand, errors in the measurement or estimation of these quantities result in shifts of λ in the opposite direction.

The intrinsically small scatter of SNe Ia is a well-suited population to constrain the MST. An intrinsic scatter of 10% in the peak brightness after light-curve width and color corrections (Scolnic et al. 2018) allows one, at least in principle, to constrain the MST to 5% in the absence of other uncertainties. Thus, glSNe are not only able to provide precise time-delay measurements owing to their transient and well-characterized nature, but at the same time SNe Ia or any other standardizable form of SNe allow one to constrain the currently dominating error budget of time-delay cosmography, the MST.

The constraints on the MST rely on precise and accurate determinations of all the parameters listed in Equation (23). The uncertainty in apparent unlensed brightness of SNe F_{unl}, millilensing $\Delta\mu_{\mathrm{milli}}$ contribution, and the microlensing effect $\Delta\mu_{\mathrm{micro}}$ are the dominant uncertainty components in constraining the MST. Systematic limitations in the usage of glSNe relate to dust extinction impacting the flux measurement F_{obs} and selection effects related to milli- and microlensing. We will review limitations and systematics of glSNE in breaking the MST in Section 5.

3. Methodology

In this section, we describe the methodology to measure H_0 from a set of glSNe by constraining the MST with the apparent magnitude distribution of an unlensed SN sample. We lay out the model assumptions and define the hyperparameters governing the cosmological expansion, SN brightness distribution, and mass profiles of the lensing galaxies. Furthermore, we detail the implementation of the likelihood for the different observations that allow us to efficiently perform a joint hierarchical sampling of the posteriors. We describe the SN Ia population assumptions and analysis in Section 3.1 and the glSN population assumptions and analysis in Section 3.2. Separately, we discuss the impact and the treatment of LOS structure in Section 3.3. In Section 3.4, we state the joint hierarchical inference problem based on the previous parts of this section. In Section 3.5, we provide an approximate analytical error propagation. The methodology presented here, in terms of parameterization and likelihood calculation, is implemented in the open-source software HIERARC.

3.1. Sn Ia Population

We focus in this work on the SN Ia population. Here we describe the SN Ia magnitude–redshift relation and the likelihood for the unlensed SN Ia sample in Section 3.1.1. In Section 3.1.2, we then state the specific model and likelihood

assumptions for the combined lensed and unlensed SNe Ia samples that we implement in this work.

3.1.1. Unlensed SN Ia Sample

SNe Ia can be standardized as precise (relative) distance indicators. This involves well-known corrections for their luminosity–width and luminosity–color relations (Guy et al. 2007, 2010). In addition, the SN Ia inferred luminosity needs to be corrected for its dependence on the host galaxy properties (e.g., stellar mass; refer to Scolnic et al. 2018, for details of the standardization procedure and bias corrections). The distance modulus, μ_{B}, relates the standardized apparent magnitude of an unlensed SN Ia, denoted as m_{B}^*, to the absolute magnitude M_{B} as

$$m_{\mathrm{B}}^* - M_{\mathrm{B}} = \mu_{\mathrm{dist}} = 5\log\left(D_L(z)\right) + 25, \qquad (24)$$

where $D_L(z)$ is the luminosity distance from the observer to the redshift of the SN and μ_{dist} is the distance modulus.

There are several large samples of the cosmological SNe Ia in the literature, e.g., Pantheon (Scolnic et al. 2018), Joint Light-curve Analysis (JLA; Betoule et al. 2014), or the Dark Energy Survey (DES; Abbott et al. 2019). For our analyses we use the largest, up-to-date compilation, i.e., the Pantheon SN Ia data set (Scolnic et al. 2018). For these SN Ia samples, covariances in the calibration parameters $\boldsymbol{\xi}_{\mathrm{sys}}$ and their evolutionary trends need to be taken into account.

Lensing magnifications, be it weak lensing from large-scale structures, strong lensing from massive deflectors, or microlensing from stars, change the flux or apparent magnitude by

$$F_\mu = \mu F \quad m_\mu = m - 2.5\log_{10}(\mu), \qquad (25)$$

where μ is the unsigned absolute magnification. For a single SN, we can formally write down the likelihood of an observed peak brightness F_{obs} given a luminosity distance D_L, lensing magnification μ, and absolute magnitude M_{B} as the likelihood of the data given a flux prediction F_{model} while marginalizing over calibration and other uncertainties, such as dust extinction, or uncertainty in the peak time, as

$$\mathcal{L}(F_{\mathrm{obs}}| D_L, \mu, M_{\mathrm{B}})$$
$$= \int \mathcal{L}(F_{\mathrm{obs}}| F_{\mathrm{model}}) p(F_{\mathrm{model}}| D_L, \mu, M_{\mathrm{b}}, \boldsymbol{\xi}_{\mathrm{sys}}) p(\boldsymbol{\xi}_{\mathrm{sys}}) d\boldsymbol{\xi}_{\mathrm{sys}}.$$
$$(26)$$

For a sample of SNe, denoted as $\mathcal{D}_{\mathrm{SNe}}$, different procedures and models have been employed for the parameterization, calibration, and marginalization of systematic errors on the population level, and we refer to the relevant work for details (e.g., Betoule et al. 2014; Scolnic et al. 2018; Abbott et al. 2019). For this work, when combining such an SN sample with glSNe, we require the likelihood $\mathcal{L}(\mathcal{D}_{\mathrm{SNe}}|\boldsymbol{\pi}, \boldsymbol{\xi}_{\mathrm{SNe}})$ of the global data set given the cosmological prediction of the luminosity distances with parameters $\boldsymbol{\pi}$ and the intrinsic brightness distribution of the SN population $\boldsymbol{\xi}_{\mathrm{SNe}}$.

To facilitate the evaluation of the likelihood, for example, Scolnic et al. (2018) compressed the marginalization in a Gaussian covariance matrix across all the measured apparent magnitudes in the SN sample as

$$\mathcal{L}(\mathcal{D}_{\mathrm{SNe}}|\boldsymbol{\pi}, \boldsymbol{\xi}_{\mathrm{SNe}})$$
$$= \frac{1}{\sqrt{(2\pi)^{n_{\mathrm{sn}}} \det(\boldsymbol{\Sigma}_{\mathbf{cov}})}} \exp\left[-\frac{1}{2}\boldsymbol{\Delta m}^{\mathrm{T}} \boldsymbol{\Sigma}_{\mathrm{cov}}^{-1} \boldsymbol{\Delta m} \right], \qquad (27)$$

where $\boldsymbol{\Delta m}$ is the difference in the observed and predicted apparent magnitude of a nonevolving intrinsic mean brightness of the SN population, n_{sn} is the length of the data vector, and $\boldsymbol{\Sigma_{\mathrm{cov}}}$ is the error covariance matrix when marginalized over the systematics variables in Gaussian form.

3.1.2. Model Parameterization and Assumptions with Pivot Magnitude

We assume, for simplicity of this work, that the intrinsic peak brightness distribution is redshift independent. This is typically assumed in cosmological analyses with SNe Ia, based on comparisons of spectroscopic and photometric properties of local and high-z SNe Ia (e.g., Petrushevska et al. 2017, and other studies of high signal-to-noise data of high-z SNe Ia).

To obtain the absolute luminosity of an unlensed SN Ia at the redshift of the glSNe in our sample would require an independent calibration of the absolute luminosity distance, e.g., as done for the distance ladder. However, since we want to derive a relative magnification at the lensed source redshift, we can use the apparent magnitude of the unlensed SNe Ia from the cosmological sample and infer it at the redshift of the lensed SN. For this, we replace using an M_{B} term with an apparent magnitude at a specific redshift, z_{pivot}, m_{p},

$$m_{\mathrm{sn}}(m_{\mathrm{p}}, z) = m_{\mathrm{p}} + 5[\log_{10} D_L(z) - \log_{10} D_L(z_{\mathrm{pivot}})]. \quad (28)$$

This parameterization results in a likelihood that is only dependent on relative distance ratios without the need of external data or constraints on top of a population of observed peak brightness of SNe. We describe the intrinsic distribution of apparent peak brightness at the pivot redshift $p(m_{\mathrm{p}})$ by a Gaussian in astronomical magnitude space with a mean $\overline{m}_{\mathrm{p}}$ and width $\sigma(m_{\mathrm{p}})$.

With these simplifications, we can write the likelihood for a single SN as

$$\mathcal{L}(F_{\mathrm{obs}}|D_L, \mu, \overline{m}_{\mathrm{p}}, \sigma(m_{\mathrm{p}}))$$
$$= \int \frac{1}{\sqrt{2\pi}\,\sigma_{\mathrm{obs}}} \exp\left[-\frac{(F_{\mathrm{obs}} - \mu F'(m_{\mathrm{p}}'))^2}{2\sigma_{\mathrm{obs}}^2} \right]$$
$$\times p(m_{\mathrm{p}}'|\overline{m}_{\mathrm{p}}, \sigma(m_{\mathrm{p}})) dm_{\mathrm{p}}', \quad (29)$$

where $F'(m_{\mathrm{p}}')$ is the shorthand form of the model predicted flux given an apparent magnitude m_{sn} calculated by Equation (28) from m_{p}' and the luminosity distance ratio, and then turned into flux units of the observations while considering the lensing magnification (Equation (25)). σ_{obs} is the Gaussian error in the flux measurements, and the term $p(m_{\mathrm{p}}'|\overline{m}_{\mathrm{p}}, \sigma(m_{\mathrm{p}}))$ in the equation above describes the likelihood of a specific pivot magnitude to be drawn from the Gaussian distribution $\mathcal{N}(\overline{m}_{\mathrm{p}}, \sigma(m_{\mathrm{p}}))$.

For an ensemble of SNe characterized with the likelihood of Equation (27), the marginalization over a Gaussian distribution in m_{p} is analytic and can directly be folded in the error covariance matrix as

$$\boldsymbol{\Sigma'_{\mathrm{cov}}} = \boldsymbol{\Sigma_{\mathrm{cov}}} + \mathrm{diag}(\sigma^2(m_{\mathrm{p}})), \quad (30)$$

and the marginalized likelihood is given by

$$\mathcal{L}(\mathcal{D}_{\mathrm{SNe}}|\boldsymbol{\pi}, \overline{m}_{\mathrm{p}}, \sigma(m_{\mathrm{p}}))$$
$$= \frac{1}{\sqrt{(2\pi)^{n_{\mathrm{sn}}} \det(\boldsymbol{\Sigma'_{\mathrm{cov}}})}} \exp\left[-\frac{1}{2}\boldsymbol{\Delta m}^{\mathrm{T}} \boldsymbol{\Sigma'^{-1}_{\mathrm{cov}}} \boldsymbol{\Delta m} \right]. \quad (31)$$

3.2. Deflector Population

We first discuss general considerations about the deflector parameterization and the necessary degrees of freedom to allow for an accurate recovery of the time-delay prediction (Section 3.2.1). We then formulate the inference problem and the general form of the joint likelihood of the imaging data, time delays, and lensed SN peak brightness observations provided by a glSN (Section 3.2.2). Lastly, we provide a Gaussian approximation of the likelihood for a fast marginalization and efficient evaluation (Section 3.2.3).

3.2.1. Deflector Parameterization and Measurements

The uncertainty in the deflector mass distribution dominates the current error budget in the H_0 inference, a statement directly reflecting the MST. A popular model describing strong gravitational lensing imaging data on galaxy-scale lenses is the power-law elliptical mass distribution (PEMD; Barkana 1998; Tessore & Metcalf 2015) combined with an external shear component. The popularity of the PEMD+shear model is a consequence of its ability to describe the data sufficiently well while keeping the degrees of freedom in the deflector model to a computationally affordable number.

Although considered simplistic, the PEMD+shear model's degrees of freedom can describe the primary azimuthal and radial observables. However, the observables in the radial direction are related to the third-order differential of the lensing potential, while the parameterization of the PEMD profile explicitly assumes a one-to-one connection between the observable invariant quantity and the mass density at the position of the Einstein ring, leading to overconstrained mass profiles and potentially biased inferences in the radial density profile, and subsequently H_0 (see, e.g., Kochanek 2002; Sonnenfeld 2018; Kochanek 2020, 2021; Birrer et al. 2020; Birrer 2021).

To mitigate possible overconstraints on the internal mass density profile, Birrer et al. (2020) added an additional degree of freedom with an MST on top of the PEMD+shear profiles of the TDCOSMO sample. A PEMD+shear+MST profile has the adequate degrees of freedom at and around the Einstein ring, where the multiple images appear, to estimate the relative Fermat potential. Higher-order differentials are subdominant in the effect on the predicted time delays (e.g., Sonnenfeld 2018). In addition, since the constraints on the MST from the lensing magnification are directly derived at the region relevant for the time-delay prediction, potential inadequacies of the PEMD+shear+MST profile further outward or toward the center of the deflector do not impact the accuracy in the inferred time-delay prediction, and thus H_0 measurement.

In this work, we assume that the population of lenses can be described by a PEMD+shear+MST profile. Furthermore, we assume that the PEMD+shear parameters can be measured accurately for each lens individually from the imaging data without population covariances, and that the MST parameter λ transforming the internal density profile of the main deflector, denoted as λ_{int}, follows a Gaussian distribution with mean λ_{int}

and sigma $\sigma(\lambda_{\rm int})$. We refer to Section 3.3 for a discussion on different MST components. We highlight that there can be physical covariances between the PEMD parameters and $\lambda_{\rm int}$, as well as among the physical projected scale and $\lambda_{\rm int}$. A possible physical projection dependence has been accounted for by Birrer et al. (2020) with an explicit parameterization of $\lambda_{\rm int}$ as a function of the ratio of deflector half-light radius relative to the Einstein radius. In this work, for the purpose of providing a forecast, we do not include secondary dependencies and covariances of $\lambda_{\rm int}$ and instead refer to Birrer et al. (2020) for the radial dependence and to Wagner-Carena et al. (2021) for a general treatment of lens model hyperparameter inferences within a hierarchical framework.

3.2.2. glSNe Inference

From the imaging data, I, we can measure the lens model parameters within our model assumptions, $\xi_{\rm pl}$, which in turn provide the Fermat potential differences between the multiple images $\Delta\tau_{\rm pl}$ and the lensing magnifications $\mu_{\rm pl}$ at the position of the appearances of the glSN. With measured relative time delays Δt and a model providing values for $\Delta\tau_{\rm pl}$, λ, and $D_{\Delta t}$, we can predict the time delay and evaluate the time-delay likelihood of the data given the model. From the same lens model, we can compute the likelihood of the measured glSN brightness F given the model prediction of $\mu_{\rm pl}$, λ, and $m_{\rm sn}$.

The joint likelihood $\mathcal{L}(I, \Delta t, F|D_{\Delta t}, m_{\rm sn}, \lambda)$ of the imaging, time delay, and flux measurements—given the relevant parameters of the hierarchical inference, $D_{\Delta t}$, $m_{\rm sn}$, and λ—can be written as a product of the likelihoods of the different independent data sets

$$
\begin{aligned}
\mathcal{L}(I, \Delta t, F|D_{\Delta t}, m_{\rm sn}, \lambda) = &\int \mathcal{L}(I|\Delta\tau_{\rm pl}, \mu_{\rm pl}) \\
&\times \mathcal{L}(\Delta t|D_{\Delta t}, \lambda, \Delta\tau_{\rm pl}) \mathcal{L}(F|m_{\rm sn}, \lambda, \mu_{\rm pl}) \\
&\times p(\Delta\tau_{\rm pl}, \mu_{\rm pl}) d\Delta\tau_{\rm pl} d\mu_{\rm pl},
\end{aligned}
\tag{32}
$$

where we explicitly marginalized over the magnification and Fermat potential parameters $\mu_{\rm pl}$ and $\tau_{\rm pl}$. To describe the imaging data I and to compute the likelihood at the pixel level, we require a lens model $\xi_{\rm pl}$ and a model of all the light components $\xi_{\rm light}$. We can describe the imaging likelihood and prior product on $\Delta\tau_{\rm pl}$ and $\mu_{\rm pl}$ as

$$
\begin{aligned}
&\mathcal{L}(I|\Delta\tau_{\rm pl}, \mu_{\rm pl}) p(\Delta\tau_{\rm pl}, \mu_{\rm pl}) \\
&= \int \mathcal{L}(I|\xi_{\rm pl}, \xi_{\rm light}) p(\Delta\tau_{\rm pl}, \mu_{\rm pl}|\xi_{\rm pl}) p(\xi_{\rm pl}, \xi_{\rm light}) d\xi_{\rm pl}\xi_{\rm light} \\
&= \int \mathcal{L}(I|\xi_{\rm pl}, \xi_{\rm light}) p(\xi_{\rm pl}, \xi_{\rm light}) \left| \frac{\partial(\Delta\tau_{\rm pl}, \mu_{\rm pl})}{\partial(\xi_{\rm pl}, \xi_{\rm light})} \right|^{-1} d\xi_{\rm pl}\xi_{\rm light}.
\end{aligned}
\tag{33}
$$

Here $\Delta\tau(\xi_{\rm pl})$ and $\mu(\xi_{\rm pl})$ are unique functions of $\xi_{\rm pl}$, and the $|\partial(\Delta\tau_{\rm pl}, \mu_{\rm pl})/\partial(\xi_{\rm pl}, \xi_{\rm light})|$ is the Jacobian determinant. This means that the likelihood and prior product of Equation (33) can be computed by sampling $\xi_{\rm pl}$ from the posterior $\mathcal{L}(I|\xi_{\rm pl}, \xi_{\rm light}) p(\xi_{\rm pl}, \xi_{\rm light})$ and evaluating for the posterior sample of the quantities $\Delta\tau_{\rm pl}(\xi_{\rm pl})$ and $\mu_{\rm pl}(\xi_{\rm pl})$. For the modeling choices and posterior sampling when marginalizing over complex source structure, we refer to previous work (e.g., Suyu et al. 2009; Birrer et al. 2015).

3.2.3. Gaussian Likelihood Approximation

Until this point in this subsection, we did not make any assumption on the form of the likelihood (Equation (32)) or on the shape of the imaging modeling posteriors (Equation (33)). To facilitate the calculation of the likelihood in Equation (32), we approximate the likelihood in Gaussian form. In particular, we write the imaging likelihood from Equation (33) as

$$
\begin{aligned}
&\mathcal{L}(I|\Delta\tau_{\rm pl}, \mu_{\rm pl}) p(\Delta\tau_{\rm pl}, \mu_{\rm pl}) \\
&\approx \frac{1}{\sqrt{(2\pi)^{n_{\Delta\tau\mu}} \det(\Sigma_{\Delta\tau\mu})}} \exp\left[-\frac{1}{2} \Delta_{\Delta\tau\mu}^{\rm T} \Sigma_{\Delta\tau\mu}^{-1} \Delta_{\Delta\tau\mu} \right],
\end{aligned}
\tag{34}
$$

where $\Delta_{\Delta\tau\mu} \equiv (\Delta\tau - \Delta\tau_0, \mu - \mu_0)$, with $(\Delta\tau_0, \mu_0)$ being the maximum likelihood estimator; $n_{\Delta\tau\mu}$ is the length of the vector $\Delta_{\Delta\tau\mu}$; and $\Sigma_{\Delta\tau\mu}$ is the error covariance matrix describing the Gaussian uncertainties in the measurement from the imaging data.

The Gaussian form of the time-delay likelihood $\mathcal{L}(\Delta t|D_{\Delta t}, \lambda, \Delta\tau_{\rm pl})$ of Equation (32) reads

$$
\begin{aligned}
&\mathcal{L}(\Delta t|D_{\Delta t}, \lambda, \Delta\tau_{\rm pl}) \\
&\approx \frac{1}{\sqrt{(2\pi)^{n_{\Delta t}} \det(\Sigma_{\Delta t})}} \exp\left[-\frac{1}{2} \Delta_{\Delta t}^{\rm T} \Sigma_{\Delta t}^{-1} \Delta_{\Delta t} \right],
\end{aligned}
\tag{35}
$$

where $n_{\Delta t}$ are the number of relative time-delay measurements, $\Sigma_{\Delta t}$ is the relative time-delay measurement error covariance matrix, and $\Delta_{\Delta t}$ is the difference between the predicted time delay (Equation (5) including an MST term of Equation (14)) and measured time delay Δt.

The Gaussian form of the flux amplitude likelihood $\mathcal{L}(F|m_{\rm sn}, \lambda, \mu_{\rm pl})$ of Equation (32) is

$$
\begin{aligned}
&\mathcal{L}(F|m_{\rm sn}, \lambda, \mu_{\rm pl}) \\
&\approx \frac{1}{\sqrt{(2\pi)^{n_F} \det(\Sigma_F)}} \exp\left[-\frac{1}{2} \Delta_F^{\rm T} \Sigma_F^{-1} \Delta_F \right],
\end{aligned}
\tag{36}
$$

where n_F is the number of flux measurements, Σ_F is the glSN flux measurement error covariance matrix, and Δ_F is the difference between the predicted peak flux of the SNe and measured flux F.

The marginalized likelihood of Equation (32) with the Gaussian approximations for the individual likelihood components (Equations (34), (35), (36)) is a Gaussian integral.

We can join the data vector of the time delays Δt and fluxes F as $d_{\Delta tF} \equiv (\Delta t, F)$ and write the joint measurement covariance matrix as

$$
\Sigma_{\rm data} = \begin{bmatrix} \Sigma_{\Delta t} & 0 \\ 0 & \Sigma_F \end{bmatrix}.
\tag{37}
$$

In this forecast, we assume no covariant measurement uncertainties between the time delays and the microlensing impact on the magnification. It has been shown that the microlensing effect on time-delay measurements can be mitigated with early-phase multicolor light curves when the microlensing effect is achromatic (Goldstein et al. 2018).

At the same time, we can transform the covariance matrix of the imaging posteriors $\Sigma_{\Delta\tau\mu}$ into the data vector space,

resulting in

$$\boldsymbol{\Sigma}_{\text{model}} = (\lambda D_{\Delta t} c^{-1} \mathbf{1}_{n_{\Delta\tau}}, \ \lambda^{-2} m_{\text{sn}} \mathbf{1}_{n_\mu}) \boldsymbol{\Sigma}_{\Delta\tau\mu}$$
$$(\lambda D_{\Delta t} c^{-1} \mathbf{1}_{n_{\Delta\tau}}, \ \lambda^{-2} m_{\text{sn}} \mathbf{1}_{n_\mu})^{\text{T}}, \tag{38}$$

where $\mathbf{1}_{n_{\Delta\tau}}$ and $\mathbf{1}_{n_\mu}$ are vectors of size $n_{\Delta\tau}$ and n_μ, respectively, with 1 at each element. The joint likelihood of Equation (32) is then given by

$$\mathcal{L}(\boldsymbol{I}, \boldsymbol{\Delta t}, \boldsymbol{F} | D_{\Delta t}, m_{\text{sn}}, \lambda)$$
$$= \frac{1}{\sqrt{(2\pi)^{n_{\Delta tF}} \det(\boldsymbol{\Sigma}_{\text{tot}})}} \exp\left[-\frac{1}{2} \boldsymbol{\Delta}_{\Delta tF}^{\text{T}} \boldsymbol{\Sigma}_{\text{tot}}^{-1} \boldsymbol{\Delta}_{\Delta tF} \right], \tag{39}$$

with $n_{\Delta tF} \equiv n_{\Delta t} + n_F$, and the total error covariance matrix being the sum of the measurement covariance and the marginalized uncertainty in the model

$$\boldsymbol{\Sigma}_{\text{tot}} = \boldsymbol{\Sigma}_{\text{data}} + \boldsymbol{\Sigma}_{\text{model}}, \tag{40}$$

and $\boldsymbol{\Delta}_{\Delta tF}$ being the difference of the data vector $\boldsymbol{d}_{\Delta tF}$ and the model prediction.

3.3. LOS Mass Distribution

Mass over- or underdensities along the LOS of the strong-lensing system cause, to first order, shear and convergence perturbations. Reduced shear distortions do have a measurable imprint on the azimuthal structure of the strong-lensing system (see, e.g., Birrer 2021), while the convergence component of the LOS, denoted as κ_{ext}, is equivalent to an MST and thus not directly measurable from imaging data. The total MST, the relevant transform to constrain for an accurate cosmography and H_0 measurement, is the product of the internal and external MST (e.g., Schneider & Sluse 2013; Birrer et al. 2016, 2020)

$$\lambda = (1 - \kappa_{\text{ext}}) \times \lambda_{\text{int}}. \tag{41}$$

The lensing kernel impacting the linear distortions, both shear and κ_{ext}, is different from the standard weak-lensing kernel (McCully et al. 2014, 2017; Birrer et al. 2017, 2020; Fleury et al. 2021b). The lensing kernel can be described as the product of three different angular diameter distances entering $D_{\Delta t}$ in Equation (7) (Birrer et al. 2020; Fleury et al. 2021a), and thus κ_{ext} can be described as the product of the individual kernels entering Equation (7) as

$$1 - \kappa_{\text{ext}} = \frac{(1 - \kappa_{\text{d}})(1 - \kappa_{\text{s}})}{1 - \kappa_{\text{ds}}}, \tag{42}$$

where κ_{d} is the weak-lensing effect from the observer to the deflector, κ_{s} is that from the observer to the source, and κ_{ds} is that from the deflector to the source (Birrer et al. 2020). Alternatively, but equivalently, the kernel can be described in the multiplane formalism with the main deflector included, while keeping the Born approximation in between (e.g., Birrer et al. 2017; Fleury et al. 2021b).

The LOS lensing contribution can be estimated by tracers of the large-scale structure, using either galaxy number counts (e.g., Greene et al. 2013; Rusu et al. 2017) or weak-lensing measurements (Tihhonova et al. 2018). These measurements, paired with a cosmological model including a galaxy–halo connection, are able to constrain the probability distribution of κ_{ext} to a few percent per LOS.

For an accurate measurement of H_0, the combined internal and external MST of Equation (42) is required. Since glSN magnification is directly probing the combined λ, the LOS

contribution effectively only adds a scatter in the inference, and an accurate overall population selection function is not required (see Birrer et al. 2020, for the same argument using kinematics to break the MST). The overall lensing selection function is only relevant when demanding a physical interpretation of the internal and external contributions separately.

In this work, for practical simplicity but without impact on expected biases or uncertainty budget, we assume a Gaussian scatter in κ_{ext} of 0.03 with a population mean at zero along the LOSs of the lenses.

3.4. Hierarchical Analysis and Sampling

Our goal is to jointly infer and marginalize over population hyperparameters in the SN distribution, lensing deflector profiles, and cosmological parameters, given the joint data set of lensed and unlensed SNe, and MST-invariant lensing quantities from imaging data. We follow the same approach as Birrer et al. (2020), except that we add the SN magnification likelihood instead of the stellar kinematic one, and as an external data set we are using a sample of unlensed SNe instead of a sample of galaxy–galaxy lenses with measured kinematics.

We want to calculate the probability of the cosmological parameters, $\boldsymbol{\pi}$, given the joint data set, $p(\boldsymbol{\pi} | \{\mathcal{D}_{\text{L}}^i\}_N, \mathcal{D}_{\text{SNe}})$, where $\mathcal{D}_{\text{L}}^i$ is the data set of an individual strong lens (including imaging data, time-delay measurements, SN flux measurement, and LOS properties), N is the total number of lenses in the sample, and $\mathcal{D}_{\text{SNe}}$ is an SN data set.

In addition to $\boldsymbol{\pi}$, we introduce $\boldsymbol{\xi}_{\text{pop}}$, which incorporates all the additional population-level model parameters not yet marginalized over the individual data sets, including their covariant impact on the likelihoods of individual lenses. Using Bayes's rule and considering that the data of each individual lens $\mathcal{D}_i$ are independent, we can write

$$p(\boldsymbol{\pi} | \{\mathcal{D}_{\text{L}}^i\}_N, \mathcal{D}_{\text{SNe}}) \propto \mathcal{L}(\{\mathcal{D}_{\text{L}}^i\}_N, \mathcal{D}_{\text{SNe}} | \boldsymbol{\pi}) p(\boldsymbol{\pi})$$
$$= \int \mathcal{L}(\{\mathcal{D}_{\text{L}}^i\}_N, \mathcal{D}_{\text{SNe}} | \boldsymbol{\pi}, \boldsymbol{\xi}_{\text{pop}}) p(\boldsymbol{\pi}, \boldsymbol{\xi}_{\text{pop}}) d\boldsymbol{\xi}_{\text{pop}}$$
$$= \int [\textstyle\prod_i^N \mathcal{L}(\mathcal{D}_{\text{L}}^i | \boldsymbol{\pi}, \boldsymbol{\xi}_{\text{pop}})] \mathcal{L}(\mathcal{D}_{\text{SNe}} | \boldsymbol{\pi}, \boldsymbol{\xi}_{\text{pop}})$$
$$\times p(\boldsymbol{\pi}, \boldsymbol{\xi}_{\text{pop}}) d\boldsymbol{\xi}_{\text{pop}}. \tag{43}$$

Table 1 summarizes the hyperparameters describing the cosmological parameters, the SN brightness distribution, and the lens population that we are sampling hierarchically. We also state the parameter priors we employ in the forecast. We refer to Birrer et al. (2020) for the formal approximation we are making in the Bayesian analysis while treating other lens model parameters independently among the different lenses and to Wagner-Carena et al. (2021) for a hierarchical analysis inferring a wider range of lens model hyperparameters.

The likelihood of an individual lens for a given set of hyperparameters, $\mathcal{L}(\mathcal{D}_{\text{L}}^i | \boldsymbol{\pi}, \boldsymbol{\xi}_{\text{pop}})$, is given by the integral of the individual parameters according to the specified distribution of the hyperparameters

$$\mathcal{L}(\mathcal{D}_{\text{L}}^i | \boldsymbol{\pi}, \boldsymbol{\xi}_{\text{pop}}) = \int \mathcal{L}(\mathcal{D}_{\text{L}}^i | \boldsymbol{\pi}, \boldsymbol{\xi}) p(\boldsymbol{\xi} | \boldsymbol{\xi}_{\text{pop}}) d\boldsymbol{\xi}, \tag{44}$$

where $p(\boldsymbol{\xi} | \boldsymbol{\xi}_{\text{pop}})$ is the distribution function of the individual parameters $\boldsymbol{\xi}$ as specified by the population parameters $\boldsymbol{\xi}_{\text{pop}}$, and $\mathcal{L}(\mathcal{D}_{\text{L}}^i | \boldsymbol{\pi}, \boldsymbol{\xi})$ is the likelihood specified by Equation (32) and its Gaussian form (Equation (39)) when stating the angular diameter distances as a function of the cosmological parameters

Table 1
Summary of the Model Parameters Sampled in Joint SN + Strong Lensing Hierarchical Inference

Name	Prior	Description
Cosmology (flat ΛCDM):		
H_0 (km s^{-1} Mpc^{-1})	$\mathcal{U}([0, 150])$	Hubble constant
Ω_m	$\mathcal{U}([0, 1])$	Current normalized matter density
Mass profile:		
$\overline{\lambda}_{\rm int}$	$\mathcal{U}([0.5, 1.5])$	Internal MST population mean
$\sigma(\lambda_{\rm int})$	$=0.03$	1σ Gaussian scatter in $\lambda_{\rm int}$
SN population:		
$\overline{m}_{\rm p}$	$\mathcal{U}([0, 30])$	Mean of the apparent magnitude distribution of the SN population at $z_{\rm pivot} = 0.1$
$\sigma(m_{\rm p})$	$=0.1$	1σ Gaussian scatter in intrinsic SN magnitude distribution at fixed redshift $m_{\rm p}$
Line of sight:		
$\overline{\kappa}_{\rm ext}$	$=0$	Population mean in external convergence of lenses
$\sigma(\kappa_{\rm ext})$	$=0.025$	1σ Gaussian scatter in $\kappa_{\rm ext}$

π. The same statement as for the lens likelihood (Equation (44)) applies for the SN sample likelihood $\mathcal{L}(\mathcal{D}_{\rm SNe}|\pi, \xi_{\rm pop})$. The marginalization in $\mathcal{L}(\mathcal{D}_{\rm SNe}|\pi, \xi_{\rm pop})$ goes over the SN brightness distribution hyperparameters $\overline{m}_{\rm p}$ and $\sigma(m_{\rm p})$. We note that the SN distribution parameters are shared for both the SN population likelihood and the individual lens likelihoods, as well as the cosmological parameters relevant to describe the relative expansion history. The absolute scales of the universe, stated in the form of H_0, only enter explicitly in the time-delay likelihood.

3.5. Analytic Error Propagation

Before we present the forecast and results with the full hierarchical sampling and propagating of the covariances in the model described in Section 3.4, we also provide an analytic, simplified, approximate error propagation. This calculation is easily accessible, is fast to compute, and provides valuable insights into the relative importance of different uncertainty components impacting the final H_0 constraints.

To first order, the relative H_0 uncertainty, σ_{H_0}/H_0, comprises the uncertainty in the population mean of the MST parameter,[10] $\overline{\lambda}$, and the uncertainty when performing an uncorrelated error propagation when fixing $\overline{\lambda} = $ const as

$$\frac{\sigma(H_0)}{H_0} \approx \sqrt{\left(\frac{\sigma(\overline{\lambda})}{\overline{\lambda}}\right)^2 + \left(\frac{\sigma(H_0)}{H_0}\right)^2_{\overline{\lambda}={\rm const}}}. \qquad (45)$$

In the following, we approximate the uncertainty budget for the distinct terms in Equation (45). For simplicity of this analysis, we assume that for all lenses, and all images, the uncertainty terms are identical. In practice, and in the full inference, inverse uncertainty weighting must be considered.

---

[10] Including internal and external MST effects.

3.5.1. Uncertainty Terms in the MST

The first term on the right-hand side of Equation (45) can be determined with absolute lensing magnifications. The population-level uncertainty in $\overline{\lambda}$ can, to first order, be expressed as the uncertainty in the population mean of the apparent unlensed brightness $\overline{m}_{\rm p}$,[11] which is covariant among all lenses, the uncertainty in the relative expansion history translating the apparent magnitude of the distribution of the external SN sample to the glSN source redshift, and uncorrelated measurement uncertainties for each individual lens (Equations (20) and (23)) as

$$\left(\frac{\sigma(\overline{\lambda})}{\overline{\lambda}}\right)^2 \approx \frac{1}{2}\left[\sigma^2(\overline{m}_{\rm p}) + \sigma^2\left(\frac{L_{z_{\rm source}}}{L_{z_{\rm SNe}}}\right) \right.$$
$$\left. + \frac{1}{N_{\rm lens}}\left(\frac{\sigma(\mu_i)}{\mu_i}\right)^2_{\overline{m}_{\rm p}={\rm const}}\right], \qquad (46)$$

where $N_{\rm lens}$ is the number of lens systems. Furthermore, for simplicity, we assumed equal precision in the individual relative magnification measurements in Equation (46) for each lens.

The relative magnification uncertainty per lens with fixed source population mean $\overline{m}_{\rm p}$ can be written, following Equation (23), as

$$\left(\frac{\sigma(\mu_i)}{\mu_i}\right)^2_{\overline{m}_{\rm p}={\rm const}} \approx \left(\frac{\sigma(F_{\rm unl})}{F_{\rm unl}}\right)^2 + \frac{1}{4}\left(\frac{\sigma(F_{\rm obs})}{F_{\rm obs}}\right)^2$$
$$+ \left(\frac{\sigma(\mu_{\rm macro})}{\mu_{\rm macro}}\right)^2 + \frac{1}{4}\left(\frac{\sigma(\Delta\mu_{\rm milli})}{\Delta\mu_{\rm milli}}\right)^2 + \frac{1}{4}\left(\frac{\sigma(\Delta\mu_{\rm micro})}{\Delta\mu_{\rm micro}}\right)^2. \qquad (47)$$

The first term on the right-hand side of the equation above is the intrinsic scatter in the standardizable source, the second is the flux measurement uncertainty, and the following ones are the different scales of the lensing effect. The factor $1/4$ comes from the fact that we consider quadruply lensed quasars, as this approximation assumes the random errors in the milli- and microlensing effects to be uncorrelated among the different images. The macro-model magnification uncertainties are covariant, and thus we omit the factor $1/4$ in the approximation.

3.5.2. Time-delay and Fermat Potential Uncertainties

The second term on the right-hand side of Equation (45) encompasses all other sources of uncertainties not related to global inference shifts due to the MST. In particular, this involves uncertainties in the time-delay measurements, the Fermat potential uncertainty for a specified mass profile family (in our case PEMD+shear) from high-resolution imaging data, and the random uncertainties in the LOS convergence estimates and the internal MST. In addition, we include in this second term uncertainties in the relative expansion history that translate the angular diameter distance measurements to the

---

[11] The differential in logarithmic astronomical magnitude m with regard to relative linear flux I is $I\partial m/\partial I = -2.5\log_{10}(e) \approx -1.086$. Thus, small scatter described in astronomical magnitudes is approximately the same scatter in relative flux.

lensing system, $D_{\Delta t}$, relative to the scales at current time, and thus H_0, which we denote as $\sigma(H_0/D_{z=\mathrm{SL}})$.

In terms of distance measurements, we can approximately write

$$\left(\frac{\sigma(H_0)}{H_0}\right)^2_{\bar{\lambda}=\mathrm{const}} \approx \frac{1}{N_{\mathrm{lens}}}\left(\left(\frac{\sigma(D^{\mathrm{pl}}_{\Delta t})}{D^{\mathrm{pl}}_{\Delta t}}\right)^2 + \left(\frac{\sigma(\lambda)}{\lambda}\right)^2\right) + \sigma^2\left(\frac{H_0}{D_{z=\mathrm{SL}}}\right), \tag{48}$$

where the relative time-delay distance measurement uncertainty can be estimated by the relative Fermat potential uncertainties from imaging modeling and the relative time-delay uncertainties,

$$\left(\frac{\sigma(D^{\mathrm{pl}}_{\Delta t})}{D^{\mathrm{pl}}_{\Delta t}}\right)^2 \approx \left(\frac{\sigma(\Delta\tau_{\mathrm{pl}})}{\Delta\tau_{\mathrm{pl}}}\right)^2 + \left(\frac{\sigma(\Delta t)}{\Delta t}\right)^2, \tag{49}$$

and the scatter and random uncertainty in λ coming from the internal and external scatter, which can be approximated as

$$\left(\frac{\sigma(\lambda)}{\lambda}\right)^2 = \left(\frac{\sigma(\lambda_{\mathrm{int}})}{\lambda_{\mathrm{int}}}\right)^2 + \left(\frac{\sigma(\kappa_{\mathrm{ext}})}{1-\kappa_{\mathrm{ext}}}\right)^2. \tag{50}$$

The time-delay distance uncertainty per lens (Equation (49)) is, to first order, a weighted product of all the different images. The random uncertainty in the MST acts as a noise term for the individual distance measurements for each lens.

4. Forecast

Having formulated the methodology and parameterization in the previous sections, we perform different forecast scenarios based on predicted number of glSNe, quality of measurements, and systematics effect. In Section 4.1 we state the expected number of glSNe and time-delay measurements and our assumptions on milli- and microlensing effects in the magnification. In Section 4.2 we state the lens model, source configuration, and uncertainties expected from imaging data on the Fermat potential and magnifications. In Section 4.3 we present the scenario for current and future unlensed SN data sets. Finally, in Section 4.4 we present the inference results for the different forecast scenarios.

4.1. Lens Population, Time-delay, and Magnification Uncertainties

In this work, we focus on the discoveries expected by the Vera Rubin Observatory LSST. We do not perform an independent forecast, and we derive our fiducial forecast scenario based on previous work in the literature.

4.1.1. Expected glSNe with LSST

Goldstein & Nugent (2017) and Goldstein et al. (2018) estimated, based on the catalog by Oguri & Marshall (2010), the number of glSNe Ia to be up to 500–900 in 10 yr of LSST with unresolved photometric magnification detection where the brightest SN image reaches a peak apparent i-band magnitude of 22.15 or brighter. Wojtak et al. (2019) compared two different discovery techniques, by magnifaction and resolved image multiplicity, and estimated the annual discovery rate

with LSST to be 61 with magnification, 44 with resolved image multiplicity, and 89 in a hybrid discovery scheme.

It has been noted that lensed SNe found via image multiplicity exhibit longer time delays and larger image separations, making them more suitable for cosmological constraints than their counterparts found via magnification (Wojtak et al. 2019; Huber et al. 2019). Huber et al. (2019) find that restricting the expected time-delay measurement to a minimum precision of <5% and an accuracy of <1% (if based solely on LSST observations) would reduce the number of lensed SNe Ia to about one per year. This rate can be increased by a factor of 216 by employing other instruments for follow-up observations. Beyond LSST, for example, Pierel et al. (2021) predict that the Roman observatory will discovery ~11 glSNe Ia. With follow-up efforts in measuring the time delays of the subsample restricted on the most promising time-delay measurements (Huber et al. 2019), LSST+follow-up is able to provide <1% overall statistical precision on H_0 from the time-delay uncertainties of 20 glSNe Ia (e.g., Suyu et al. 2020).

4.1.2. Milli- and Microlensing

Milli- and microlensing effects on the magnification of the glSNe can significantly impact the ability of glSNe to be used as standardizable candles. Millilensing is an effect caused by dark subhalos of the main deflector or along the LOS (e.g., Dalal & Kochanek 2002; Gilman et al. 2020a; Hsueh et al. 2020) or baryonic effects (e.g., Hsueh et al. 2016; Gilman et al. 2017). Flux ratio anomalies at the ~10% level have been studied and used to constrain dark matter properties with quadruply lensed quasar flux ratio anomalies (e.g., Gilman et al. 2020a; Hsueh et al. 2020). For the physical source size of SNe, Kelly et al. (in preparation) estimated for SN Refsdal (Kelly et al. 2015) a ~10% scatter from millilensing based on the forward-modeling methodology by Gilman et al. (2019, 2020a).

Microlensing caused by stars or other compact objects in the foreground lensing galaxy or along the LOS can be a more significant limit to the standardization of glSNe. Microlensing can independently magnify or demagnify individual images of the background source (Dobler & Keeton 2006; Bagherpour et al. 2006), introducing scatter into the shape and amplitude of the resulting light curves. The effect of microlensing on each lensed image depends on the local smooth lensing properties (convergence κ, shear γ) and the stellar (or compact) projected mass fraction κ_*/κ. For example, Schechter & Wambsganss (2002) investigated stellar microlensing effects on lensed quasars at image magnifications of $\mu \sim 10$ with moderate compact object mass fractions and showed that for such scenarios the expected microlensing scatter can result in more than an astronomical magnitude. Yahalomi et al. (2017) investigated microlensing in iPTF16geu and concluded that the scatter results in 0.73 mag from the microlensing effect alone. All in all, microlensing poses significant limits to the utility of glSNe in being used as a probe of standardizable magnification.

Foxley-Marrable et al. (2018), with the aim of assessing glSNe Ia to be standardizable in the same spirit as this work, evaluated the effect of microlensing on glSNe Ia for various image configurations. They found that there are regions of parameter space where the effect of microlensing is suppressed enough for the glSN Ia to be standardizable. Specifically, regions of low κ, low γ, and high s are subject to microlensing

scatter of $\sigma_{ML} \sim 0.15$ in astronomical magnitude, particularly at early times. Physically, this corresponds to asymmetric configurations with at least one image located far outside the Einstein radius, which will experience the least amount of microlensing.[12]

When Foxley-Marrable et al. (2018) combined their microlensing models with the glSN Ia catalog from Goldstein & Nugent (2017), they predicted that $\sim$22% of the $\sim$930 glSNe Ia to be discovered by LSST will be standardizable ($\sigma_{ML} \sim 0.15$ or below for at least one image). The standardizabe sample has a median maximal time delay of 44 days and consists of a 5:1 ratio of doubles versus quads. Foxley-Marrable et al. (2018) further concluded that from their sample of 650 glSNe Ia, of which accurate time delays can be measured, the MSD can be broken at the 0.5% level when considering microlensing and intrinsic scatter of the SNe as the source of statistical uncertainties.

4.1.3. Specific Numbers and Uncertainties of This Forecast

Overall, restricting the follow-up effort to a considerably smaller number than the overall expected discoveries optimized to derived time-delay precision and accuracy, LSST is expected to provide sufficient statistical precision on time delays with a subpercent error budget on final H_0 constraints. However, using glSNe for standardizable magnification constraints may require a larger and potentially different subset of the glSN Ia population to be further investigated with follow-up efforts. Given that the mass profile uncertainties are at the 10% level for individual lenses, we consider in this forecast a scenario with an extended sample of glSNe Ia beyond the subset of Huber et al. (2019) and Suyu et al. (2020) with lower-precision time-delay measurements, including glSNe with both shorter time delays and fainter images.

In this forecast, we design a scenario where time-delay precision and the standardizable nature of glSNe Ia can be utilized. We stress that time-delay measurement and flux standardization do not necessarily need to come from the same lenses.[13]

We chose a lens population roughly following Foxley-Marrable et al. (2018). In total, we perform our forecast with 144 glSNe, among which 24 are quads and 120 are doubles. For the quad population, we split the sample into eight crosses, eight cusps, and eight fold configurations.[14] The doubles we split into three different configurations each consisting of 40 systems.

For the redshift distribution, we assume a uniform distribution of the deflector redshift, z_{lens}, between $z = 0.1$ and $z = 0.5$, and for the source redshift, z_{source}, a uniform distribution in $\mathcal{U}[z_{lens} + 0.2, 1.]$, similar to the distribution by Huber et al. (2019) and Suyu et al. (2020) restricting to the brighter population for both accurate time-delay and flux measurements. We stress the importance of rapid spectroscopic follow-up to confirm the SN type, and we assume that the follow-up has been acquired for the SN sample and the SNe have been robustly typed.

For the time-delay measurement, we assume that the light curves can be resolved in follow-up observations and the relative time delays can be measured with a precision of 2 days per image pair.[15] Along with spectroscopy obtained for the typing, these cadenced observations provide further evidence to distinguish the normal SNe Ia from peculiar subtypes (see, e.g., Taubenberger 2017, for review), since fast-declining and super-Chandra subtypes do not show a second maximum in the near-IR (NIR), unlike normal SNe Ia. The presence of an NIR second maximum was further confirmation that iPTF16geu is a normal SN Ia (Dhawan et al. 2020). In addition to precise time delays, obtaining resolved photometry, in multiple wave bands, is crucial for constraining the extinction properties. We assume that, similar to the case for iPTF16geu, there are cadenced observations in multiple optical and NIR filters to constrain the extinction in the host galaxy and the individual LOSs in the lens for each image (Dhawan et al. 2020). Accounting for extinction correction, the magnification is inferred robustly with small uncertainties, making it a subdominant contribution to other sources.

For the flux uncertainty at peak brightness for the individual images, we use an effective relative magnitude uncertainty $\sigma_{eff}(m)$ that includes possible uncertainties from small scale milli- and microlensing effects

$$\sigma_{eff}^2(m) \equiv \left(\frac{\sigma(F_{obs})}{F_{obs}}\right)^2 + \left(\frac{\sigma(\Delta\mu_{milli})}{\Delta\mu_{milli}}\right)^2 + \left(\frac{\sigma(\Delta\mu_{micro})}{\Delta\mu_{micro}}\right)^2. \tag{51}$$

This is a practically convenient noise definition when assuming Gaussian uncorrelated error in terms of the uncertainty relevant to constraining the MST. Beyond the intrinsic scatter in the SN population, $\sigma(m_p)$, and the uncertainty in the macro-model magnification, $\sigma(\mu_{macro})$, the term in Equation (51) above can play a dominant role in the uncertainty budget and is by itself uncertain given the current rare discoveries and follow-up data of glSN systems.

We separate the $\sigma_{eff}(m)$ term for the different images into one image denoted as the standardizable one, $\sigma_{eff, std}(m)$, and all other images denoted as the microlensing dominated ones, $\sigma_{eff, ML}(m)$. For $\sigma_{eff, ML}(m)$ we assume a scatter of one magnitude, $\sigma_{eff, ML}(m) = 1.0$, making most images of glSNe inefficient probes of the mass profile.

For the "standardizable image" we perform three different scenarios for $\sigma_{eff, std}(m)$. The first scenario, denoted as IDEAL, sets $\sigma_{eff, std}(m) = 0$ for all measurements, assuming no milli- and microlensing effects and perfect flux measurements. The IDEAL scenario is meant to assess the error budget and the precision floor of any other uncertainty component. The second scenario, denoted as REALISTIC, sets $\sigma_{eff, std}(m) = 0.2$ for all measurements. The REALISTIC scenario represents a likely scenario for the uncertainty terms contained in $\sigma_{eff, std}(m)$. A specific split among its constituents is not required but is motivated by a $<$10% flux measurement uncertainty, a $\sim$10% millilensing uncertainty, and a $\sim$15% microlensing uncertainty. The third scenario, denoted as EXTREME, sets $\sigma_{eff, std}(m) = 1$, a

---

[12] We also refer to Weisenbach et al. (2021) for the reverse investigation of the configuration with the largest magnification scatter due to microlensing.

[13] The lenses need to be self-similar to translate the MST breaking to the time-delay lenses.

[14] This split is not based on ability of standardizable magnifications but primarily for pedagogic illustration.

[15] We refer to Equation (49) for the impact on the statistical error propagation with different time-delay precision. Overall, in this forecast the time-delay measurement uncertainties are subdominant to other sources of uncertainties.

Table 2
glSN Forecast Scenarios in Terms of Numbers of glSNe, Their Redshift
Distribution, and Measurement Uncertainties

Number of glSNe:		
Cusp	8	
Cross	8	
Fold	8	
Doubles	40+40+40	
Total	144	
Redshift distribution:		
z_{lens}	$\mathcal{U}[0.2, 0.5]$	Deflector redshift
z_{source}	$\mathcal{U}[z_{\text{lens}} + 0.2, 1.0]$	Source redshift
Measurement uncertainties (1σ):		
$\delta\Delta t$	± 2.0 days	Time-delay precision
σ_{eff}	Effective magnitude precision (Equation (51))	Scenario
$\sigma_{\text{eff, std}}$	± 0.0	IDEAL
$\sigma_{\text{eff, ML}}$	± 1.0	
$\sigma_{\text{eff, std}}$	± 0.2	REALISTIC
$\sigma_{\text{eff, ML}}$	± 1.0	
$\sigma_{\text{eff, std}}$	± 1.0	EXTREME
$\sigma_{\text{eff, ML}}$	± 1.0	

Note. The parameters of the macro model and their uncertainties for the forecast are presented in Table 3. The effective magnitude precision (Equation (51)) is split between one image that is less affected by microlensing ($\sigma_{\text{eff, std}}$) and the other images that are more strongly affected by microlensing ($\sigma_{\text{eff, ML}}$).

scenario where the magnification of every single image of a glSN is dominated by small-scale microlensing magnification. We highlight that these uncertainty terms should be interpreted as statistical averages for the population of glSNe. In particular, the microlensing component is expected to vary from image to image substantially depending on the stellar surface brightness.

Table 2 summarizes our choices for the forecasts presented in this work. We emphasize that our forecast scenario and numbers operate under the assumption of imminent and complete follow-up observation after a discovery or promising candidate. The total number and numbers per year may be lower with the dedicated follow-up, and we provide an extended forecast prediction as a function of glSNe in Section 4.5.

4.2. Deflector Model

The model parameters for the PEMD+shear model are described in Table 3. We chose the same lens model for all glSN systems for simplicity, but with general application of the error propagation and uncertainties. The different source positions of the glSNe for the cusp, cross, and fold configurations are also provided in Table 3. We mimic high-resolution imaging data constraints on the lens model parameters with Gaussian errors on the lens model parameters, also stated in Table 3. For the image positions of the multiply lensed SNe, we assume an astrometric precision of ± 0.005 arcseconds, achievable with high-resolution imaging around SN peak brightness. Birrer & Treu (2019) highlighted the

Table 3
Deflector Model Parameters and Uncertainties for the Forecast

Parameter	Value	Description
Lens Model (PEMD+shear)		
θ_{E}	1.0 ± 0.02	Einstein radius [arcsec]
γ_{pl}	2.00 ± 0.03	Power-law slope
e_1	0.30 ± 0.01	Eccentricity of deflector
e_2	-0.01 ± 0.01	Eccentricity of deflector
x_0	0.00 ± 0.01	Center of deflector [arcsec]
y_0	0.00 ± 0.01	Center of deflector [arcsec]
γ_1	0.05 ± 0.01	External shear component
γ_2	0.00 ± 0.01	External shear component
Image Configurations		
(x_s, y_s)	$(0.15, 0.00)$	cusp source position [arcsec]
(x_s, y_s)	$(0.02, 0.00)$	cross source position [arcsec]
(x_s, y_s)	$(0.05, 0.10)$	fold source position [arcsec]
(x_s, y_s)	$(0.05, 0.40)$	double#1 source position [arcsec]
(x_s, y_s)	$(0.20, 0.20)$	double#2 source position [arcsec]
(x_s, y_s)	$(0.40, 0.20)$	double#3 source position [arcsec]
$\delta\theta_{\text{image}}$	± 0.005	astrometric precision [arcsec]

Note. The parameters correspond to the PEMD+shear model. The uncertainties represent high-resolution imaging data modeling uncertainties when the SN is faded away.

importance and requirements on the astrometric precision of the images of the time-variable sources. Our chosen precision meets the requirement not to be the dominant uncertainty in our inference.

We sample the posterior of the imaging data (Equation (33)) with the Gaussian likelihood in the lens model and image position parameters while demanding the image positions originating from the same source position for the proposed lens model as a solution of the lens equation. We then transform the posteriors into the relative Fermat potential and absolute magnifications at the predicted image positions (Equation (33)).

The joint relative Fermat potential and magnification posteriors for the cusp configuration are illustrated in Figure 1. Similar posterior products are derived for the cross and fold configurations and are presented in the Appendix (Figures 5, 6).

The effective macro-model magnification uncertainty is ~5% per image. The effective relative Fermat potential uncertainty is ~4% per image pair. The uncertainties are comparable for the three different image configurations chosen in this forecast and compatible with uncertainties obtained from the analysis of real data by the H0LiCOW/SHARP/STRIDES/TDCOSMO collaborations (Suyu et al. 2010, 2013; Wong et al. 2017; Birrer et al. 2019; Chen et al. 2019; Rusu et al. 2020; Shajib et al. 2020). The posteriors in Fermat potential and magnification for our chosen configurations and uncertainties are well approximated by multivariate Gaussians, which justifies the use of the Gaussian likelihood of Equation (34) with the covariance matrix $\Sigma_{\Delta\tau\mu}$.

4.3. Unlensed Field SN Data Set

The data set of unlensed (field) SNe fulfills two purposes. First, it anchors the apparent unlensed population of SNe, $\overline{m}_{\text{p}}$ and $\sigma(m_{\text{p}})$, and their uncertainties. The parameter $\overline{m}_{\text{p}}$ directly translates to $\overline{\lambda}$, and thus to H_0. Second, the relative luminosity
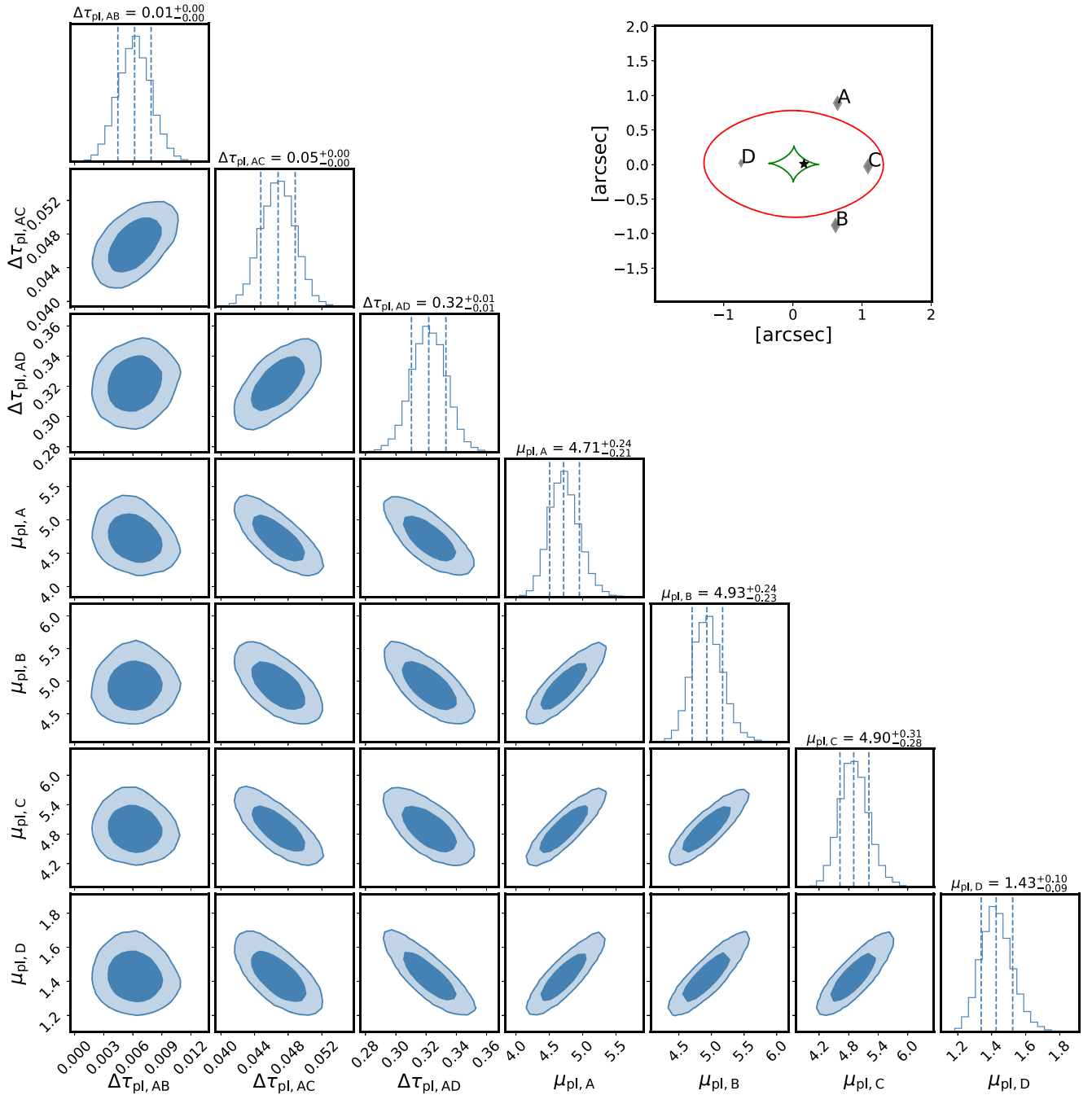
Figure 1. Mock image modeling posterior on the relative Fermat potential and lensing magnification between the image positions of a glSN when fit by a PEMD +shear lens model for the cusp configuration. The lens model parameters and uncertainties are presented in Table 3. The configurations of the image position (diamonds), inner caustic (green), and critical curve (red) are illustrated in the top right panel. The posteriors for the cross and fold configurations are presented in the Appendix.

distances of SNe constrain the relative expansion history of the universe, and thus $\Omega_{\rm m}$ in flat ΛCDM. The uncertainty on the relative expansion history can have two ways to impact the resulting H_0 uncertainty: (i) the translation of the distance measurement corresponding to the glSN systems at intermediate redshifts to the local distance constraints for a given MST parameter $\overline{\lambda}$ (Equation (48)), similar to an inverse distance ladder; and (ii) the translation of the apparent magnitudes from the distribution of unlensed (mostly lower redshifts) to the glSN source redshifts (mostly higher redshifts; Equation (46)).

To assess current and future uncertainties coming from field SN data sets, we set up two scenarios. First, we utilize the Pantheon data set (Scolnic et al. 2018). In particular, we are using the full covariance matrix product as described by Scolnic et al. (2018). The covariance matrix includes the intrinsic scatter in the SN Ia distribution, as well as covariant systematic uncertainties. Second, we mimic a future SN data set with an anticipated increase in the sample and lowering of systematics over the coming 10 yr with the onset of the Roman Space Telescope. We use the forecast covariance matrix by Hounsell et al. (2018). The comparison between the

Table 4
Summary of Constraints Provided by the Two Field SN Samples Used in the Forecast, the Pantheon Sample by Scolnic et al. (2018) and a Forecast for the Roman Space Telescope by Hounsell et al. (2018)

Scenario	Ω_{m}	$\overline{m}_{\mathrm{p}}$	$\sigma(m_{\mathrm{p}})$
PANTHEON	$0.299^{+0.023}_{-0.022}$	$18.966^{+0.008}_{-0.008}$	$=0.1$
ROMAN	$0.300^{+0.005}_{-0.004}$	$18.966^{+0.005}_{-0.004}$	$=0.1$

hierarchical glSN inference with the current Pantheon sample and the future SN sample allows us to emphasize the importance of the field SN sample in the next decade to utilizing glSNe to their full potential.

Table 4 provides the one-dimensional marginal constraints on Ω_{m} and $\overline{m}_{\mathrm{p}}$ derived from the two samples.

4.4. Forecast Results

We perform the hierarchical analysis of the parameters and their priors presented in Table 1. We make use of the Gaussian likelihoods of individual glSNe as presented in Section 3, with the numbers of glSNe and uncertainties presented in Tables 2 and 3. We specified three different uncertainty scenarios for $\sigma_{\mathrm{eff,\ std}}(m)$ (Equation (51), Section 4.1.1), IDEAL (0.0), REALISTIC (0.2), and EXTREME (1.0). We also specified two different unlensed SN scenarios, PANTHEON and FUTURE (Table 4). Any combination of SN sample and $\sigma_{\mathrm{eff,\ std}}(m)$ uncertainties results in six forecast scenarios. Figure 2 shows the posterior inference with the scenarios of the PANTHEON sample. Figure 3 shows the same inferences with the ROMAN sample.

In addition to these six inferences with a fully covariant MST component in the deflector model, we perform, as a reference for the time-delay and PEMD+shear lens model uncertainties, the forecast also without a covariant MST component by fixing $\overline{\lambda}_{\mathrm{int}} = 1$ for both SN scenarios. The scenarios without the MST do not depend on the error budget of the lensing magnifications $\sigma_{\mathrm{eff}}(m)$ and the difference in the unlensed SN sample, and the glSN sample only impacts the translation of the distance measurements into H_0. Table 5 summarizes the results with regard to the relative precision on H_0 for the eight different scenarios considered in this work.

First, ignoring the MST, the mock data of measured time delays and Fermat potential allow one to constrain H_0 to 0.5% precision with both the PANTHEON and ROMAN samples. This set of forecasts serves as a statistical reference and does not require standardizable magnifications to add information.

Once the MST is let free and only constrained by the magnifications, both the impact of the uncertainties of $\sigma_{\mathrm{eff}}m$ and the external SN sample significantly impact the resulting constraints. The difference between the constraining power of the PANTHEON and ROMAN samples can be seen prominently when comparing the scenarios with $\sigma_{\mathrm{eff,\ ml}}m = 0$, the IDEAL case without microlensing. The PANTHEON inference results in a precision of 0.8%, while the increased constraining power of the ROMAN sample results in a 0.6% precision on H_0. The error budget of the PANTHEON_IDEAL scenario is dominated by uncertainties in the unlensed SN population, whereas the ROMAN_IDEAL achieves almost the same precision as a scenario without an MST uncertainty.

When including REALISTIC or even EXTREME microlensing uncertainties in our forecast, the uncertainties in $\overline{\lambda}_{\mathrm{int}}$ start dominating the constraining power on H_0 as expected from the

constraining power on the magnification constraints (Equations (46) and (47)). Overall, we highlight our fiducial future scenario, ROMAN_REALISTIC, which provides a 0.9% precision measurement on H_0 with a full 10 yr LSST survey paired with a ROMAN SN sample.

4.5. Generalized Forecast and Expected Time Line

Overall, the results of the full hierarchical inference performed in Section 4.4 can be well approximated with the analytical error propagation terms of Section 3.5. In this section, we make use of the analytic error propagation and generalize the forecast results of Section 4.4 for a range in the number of glSNe.

Figure 4 shows the expected relative precision on H_0 as a function of the number of glSNe to be expected in the future for the three different microlensing scenarios and the two different external SN samples considered in this work. In about 2 yr of the LSST survey when expecting $\sim$28 glSNe, we forecast for the REALISTIC scenario a $\sim$3% precision on H_0. With $\sim$150 glSNe for the ROMAN_REALISTIC scenario we expect a 1% precision on H_0. The precision of the external SN sample substantially impacts the total error budget on H_0 for $>$50 glSNe in the REALISTIC scenario. These numbers in terms of years of LSST survey assume an optimal follow-up effort of the discovery candidates.

5. Discussion

The forecast results presented in Section 4 only covered a limited range of possible systematics and opportunities regarding studying glSNe and measuring H_0. In this section, we discuss key systematics, as well as other windows of opportunities, and give some general recommendations driving the design requirements in future studies of glSNe to achieve a sub-2% precision and accuracy of an H_0 measurement.

5.1. Systematics

5.1.1. Selection Effects

Brightness selection effects in the discovery and follow-up analysis of glSN systems may pose significant limitations in the standardizable magnification methodology. Bright glSNe are easier to discover and to follow up on. Such a selection can impact unlensed brightness selection, as well as local lensing magnification selection.

In our forecast and methodology, we assume an identical unlensed peak SN brightness distribution for the unlensed field sample and for the glSN population ($\overline{m}_{\mathrm{p}}$). Unaccounted-for differences between the unlensed field sample, $\overline{m}_{\mathrm{p,\ field}}$, and the glSN sample, $\overline{m}_{\mathrm{p,\ glSNe}}$, result in a differential shift in H_0 by

$$\frac{\delta H_0}{H_0} = \frac{1}{2}(\overline{m}_{\mathrm{p,\ glSNe}} - \overline{m}_{\mathrm{p,\ field}}). \tag{52}$$

Thus, an unaccounted-for relative selection effect of the field SNe and glSNE of 2% results in a 1% bias in H_0. Or in terms of an error budget, an uncertainty in the relative magnitude selection effect of 2% results in an additional error term of 1% on H_0 on top of the presented forecast results in Section 4.

Local lensing magnification, a combination of micro-, milli-, and macrolensing effects, may overall dominate the brightness selection. In particular, large (up)scatter in brightness for rare microlensing events could significantly impact the selection
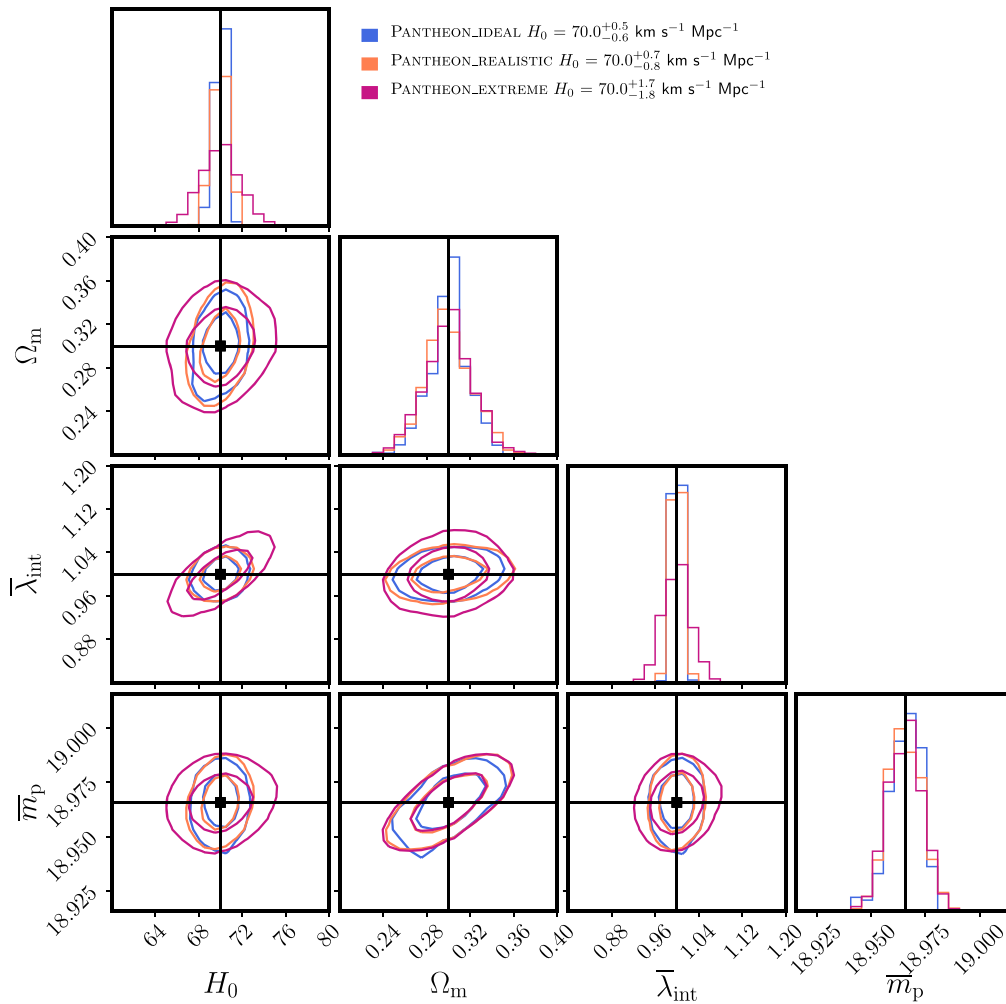
Figure 2. Posterior inference for the forecast of 144 glSNe of the parameters and their priors presented in Table 1 (see also Tables 2 and 3 for details on the uncertainties) with the Pantheon unlensed SN sample. We specified three different uncertainty scenarios for $\sigma_{\mathrm{eff,\,std}}(m)$ (Equation (51), Section 4.1.1), IDEAL (blue; 0.0), REALISTIC (orange; 0.2), and EXTREME (violet; 1.0). Figure 3 presents the same forecast with a Roman unlensed SN sample.

function. It is thus crucial to understand the microlensing selection effect. Macrolensing selection biases are less of an issue when performing the cosmographic analysis with time delays obtained by the identical selection function. However, when applying inferred mass profile constraints to lenses with different selection criteria, such as lensed quasars, the relative selection function comes into play.

5.1.2. SN Dependence with Redshift and Host Galaxies

Beyond the glSN systems and the required understanding of their selection function, breaking the MST and measuring H_0 also rely on an accurate and precise relative luminosity distance and intrinsic SN distribution derived by an unlensed SN data set. Such data sets are also used as a stand-alone cosmological probe or as a key component of a combined cosmological probe analysis, and their requirements and precision impact a glSN+SN analysis, as presented in this work.

For example, strong ~0.1–0.2 mag dependence on the local host galaxy UV surface brightness, as reported by Rigault et al. (2015), needs to be understood when making inferences from high-redshift SNe Ia. However, if there are reliable apparent magnitudes for unlensed field SNe available at the same redshifts as the glSNe, this can circumvent systematics limiting

an SN sample in measuring the late-time relative expansion history of the universe.

We also note that with increased distance (higher redshifts) lensing effects also increasingly affect the apparent magnitudes of the field SN sample as well. Relative selection effects (see Section 5.1.1) also need to consider lensing selection effects in the field SN sample.

We note that it is well known that the dust properties of SN Ia hosts, parameterized by the total-to-selective absorption ratio, R_V, are very diverse and differ from the canonical value of the Milky Way of $R_V = 3.1$ (see, e.g., Brout & Scolnic 2021; Thorp et al. 2021; Johansson et al. 2021, for recent studies). Therefore, we require multiband data for each glSN in our sample to constrain the R_V and color excesses in the host and lens galaxies. This is important since unresolved photometry alone has been shown to underestimate the inferred magnification, as seen for iPTF16geu (Goobar et al. 2017; Dhawan et al. 2020), mandating the need for optical and NIR coverage for each image of the glSN.

5.1.3. Gaussian Uncertainty Approximations

In the forecast of this work, we assumed Gaussian uncertainties in the measurements (linear flux units), lognormal scatter in the intrinsic SN peak brightness distribution, and
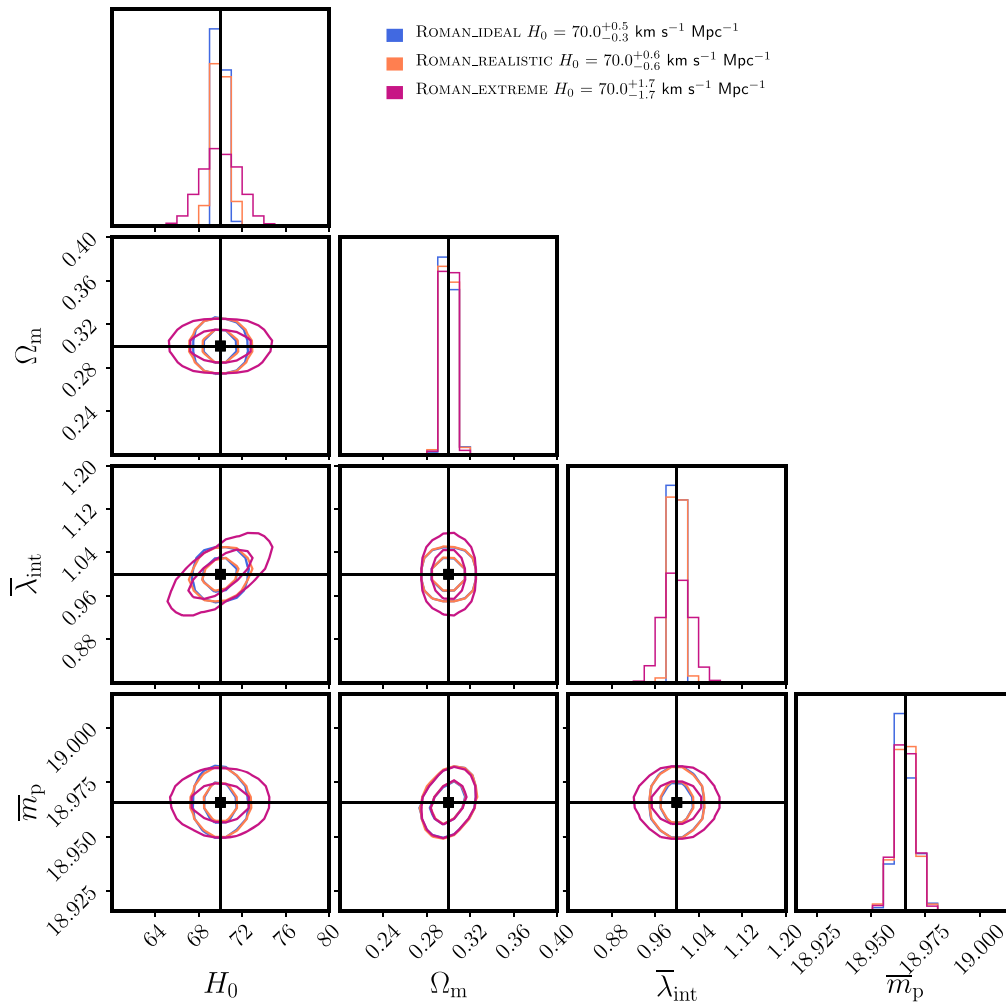
Figure 3. Posterior inference for the forecast of 144 glSNe of the parameters and their priors presented in Table 1 (see also Tables 2 and 3 for details on the uncertainties) with a Roman unlensed SN sample (Table 4). We specified three different uncertainty scenarios for $\sigma_{\mathrm{eff,\,std}}(m)$ (Equation (51), Section 4.1.1), IDEAL (blue; 0.0), REALISTIC (orange; 0.2), and EXTREME (violet; 1.0). Figure 2 presents the same forecast with the current Pantheon unlensed SN sample.

Gaussian scatter in the milli- and microlensing magnifications. The tails of the distributions need to be accurately captured to guarantee an unbiased joint inference.[16] In the current forecast, we explicitly distinguish between logarithmic and linear units and Gaussian likelihoods in either magnitude or flux units. This is not meant to be accurate for any specific scenario but primarily to emphasize the importance of accurately describing a likelihood or a posterior product. Further care and emphasis must be undertaken in describing the probability density function (pdf) of the different components of the lensing magnifications. Specifically, non-Gaussian tails in the distributions, when combining a large set of glSNe, may significantly impact the resulting posterior pdf. The hierarchical sampling and marginalization over population distributions further pose challenges in the accuracy of the likelihood evaluation and computational requirements. Gaussian or multivariate Gaussian distributions have the advantage of analytic solutions for marginalizations and likelihood evaluations, but the assumptions of Gaussian pdfs need to be tested to meet the requirement of an accurate combined posterior inference.

5.2. Opportunities

Aside from additional potential systematics considerations, there are also opportunities and circumstances that might increase the resulting precision on H_0 from glSNe relative to our fiducial forecast scenario. This section lists and briefly discusses a few of those opportunities.

5.2.1. glSNe without a Time Delay

The expected number of glSNe derived by Huber et al. (2019) that we adopt in our forecast is, in part, based on the requirement to achieve a time-delay measurement. There are potentially many more glSNe expected to be discovered (see, e.g., Goldstein et al. 2019) where a precise time-delay measurement might not be expected. However, the availability of measured time delays is not the dominant source of uncertainty in our forecast. The primary information requirement to improve constraints on H_0 is foremost a precise absolute magnification measurement.

5.2.2. Galaxy–SN Lensing

There is also a set of "semi-strongly" lensed SNe expected with a single magnified image available that is lensing through the outskirts of a lensing galaxy. An absolute magnification

---

[16] See, e.g., Section 4.4 of Park et al. (2021) for a discussion on tails in the external convergence distributions impacting combined constraints on H_0 for 200 quasar lenses.

Table 5
Summary of the Achieved Precision on H_0 for the Six Forecast Scenarios of This Work, and the Two Scenarios When Keeping $\overline{\lambda}$ Fixed

Scenario	SN Sample	$\sigma_{\mathrm{eff,\ std}}(m)$	$\sigma_{\mathrm{eff,\ ml}}(m)$	$\delta H_0/H_0$
PANTHEON_NO_MST	Pantheon	⋯	⋯	0.6%
PANTHEON_IDEAL	Pantheon	0.0	1.0	0.8%
PANTHEON_REALISTIC	Pantheon	0.2	1.0	1.1%
PANTHEON_EXTREME	Pantheon	1.0	1.0	2.5%
ROMAN_NO_MST	Roman SNe	⋯	⋯	0.6%
ROMAN_IDEAL	Roman SNe	0.0	1.0	0.6%
ROMAN_REALISTIC	Roman SNe	0.2	1.0	0.9%
ROMAN_EXTREME	Roman SNe	1.0	1.0	2.4%

Note. We specified three different uncertainty scenarios for the standardizable image $\sigma_{\mathrm{eff,\ std}}(m)$ (Equation (51), Section 4.1.1), IDEAL (0.0), REALISTIC (0.2), and EXTREME (1.0). We also specified two different unlensed SN scenarios, PANTHEON and FUTURE (Table 4). Any combination of SN sample and $\sigma_{\mathrm{eff}}(m)$ uncertainties results in six forecast scenarios. The resulting posterior inference on H_0 is given in the last row. The posteriors are also presented in Figures 2 and 3 for the PANTHEON and FUTURE SN sample, respectively.

measurement remains possible in the absence of multiple images, and such an enhanced sample might provide significant information on the more extended galaxy density profile, thus also constraining the physically plausible MST components (see, e.g., Rodney et al. 2015, for such an analysis with a singly lensed SN in a cluster environment). Such a probe is conceptually similar to galaxy–galaxy lensing and can possibly enhance the signal-to-noise ratio in the very innermost scales of galaxies, where galaxy shape information is less accessible and nonlinear perturbations may arise on the distortion of the shapes (see, e.g., Coupon et al. 2013, for work using magnifications of galaxies for such type of analysis).

5.2.3. Other Types of Standardizable Sources

Our forecast has focused on SNe Ia, in terms of the expected numbers, intrinsic scatter, and light-curve properties, to measure a peak brightness and a time delay. There are other transient sources that can be standardizable. Different studies succeeded in constructing a Type II SN Hubble diagram with a dispersion of ~10%–14% in distance (e.g., Nugent et al. 2006; Poznanski et al. 2010; de Jaeger et al. 2015). The more abundant Type II SNe may provide a valuable addition. Though the light curves of Type II SNe are not as suited for time-delay measurements as with SNe Ia, there might be advantages in measuring an absolute magnification effect with Type II SNe.

Beyond SNe, there are also gravitational waves (GWs) that can be standardized remarkably well and thus may open up opportunities beyond the capabilities of SNe. Repeated fast radio bursts (FRBs) may also provide the possibility for a standardization. For GWs and FRBs, one challenge will be the required astrometric precision to precisely determine the Fermat potential and macro-model magnification (see, e.g., Birrer & Treu 2019).

5.2.4. Constraints from Stellar Kinematics

In our forecast, we left out anticipated constraints from stellar dynamics measurements on density profiles and breaking the MST, in part because there is a larger literature on stellar kinematics in breaking the MST and existing recent literature providing a forecast for this methodology for the decade to come (Birrer & Treu 2021). Another reason is to assess a kinematic-independent methodology in breaking the MST, and thus constraints on the MST can be combined, provided that both kinematics and standardizable

magnifications are consistent. We highlight that stellar kinematic measurements can be performed on the glSN lenses once the glSNe have faded away and thus might provide similar, but independent, constraining power per glSN. Given that both methodologies are expected to provide about 1.5% precision on H_0 in the next decade, this can result in stringent consistency checks and mitigation of currently nonanticipated systematics effects and establish a precise direct distance anchor of the universe.

5.3. Recommendations

Based on our forecast and the discussion of possible systematics and opportunities, we provide here some recommendations for the community to help guide successful future strategies in providing both accurate and precise measurements of H_0 with glSNe. We focus on some aspects that either emerged directly from this work or deserve special emphasis.

1. *Perform follow-up observations for standardizable glSN candidates regardless of the expected time-delay precision.* The precision on the mass profiles and hence H_0 relies on the ability of standardizable magnifications. Among the glSN Ia discoveries, those systems with low expected microlensing events are the most valuable in breaking the MST. A significant number of glSNe Ia where at least one image is at lower magnification and lower projected stellar density are necessary, regardless of the time-delay precision (see also Foxley-Marrable et al. 2018). It is thus important to allocate significant follow-up efforts for those glSNe to be able to perform the analysis as forecasted in this work.

2. *Integrate weak- and strong-lensing SN analysis.* To some extent, the division of the field SN sample and the glSN sample is an artificial cut in an underlying population of SNe that get lensed. Most lensing is weak with few percent magnification, while the tails in the lensing magnification are effectively leading to glSNe. It is important to characterize the lensing effects across the entire spectrum to accurately describe the relative selection effects. With a more distant SN sample, lensing effects may inevitably become more prominent also for the field SN sample.

3. *glSN discovery strategy must provide a reproducible selection function.* Relative selection effects are possibly a dominant source of uncertainty or unaccounted-for systematics. Making use of the standardizable
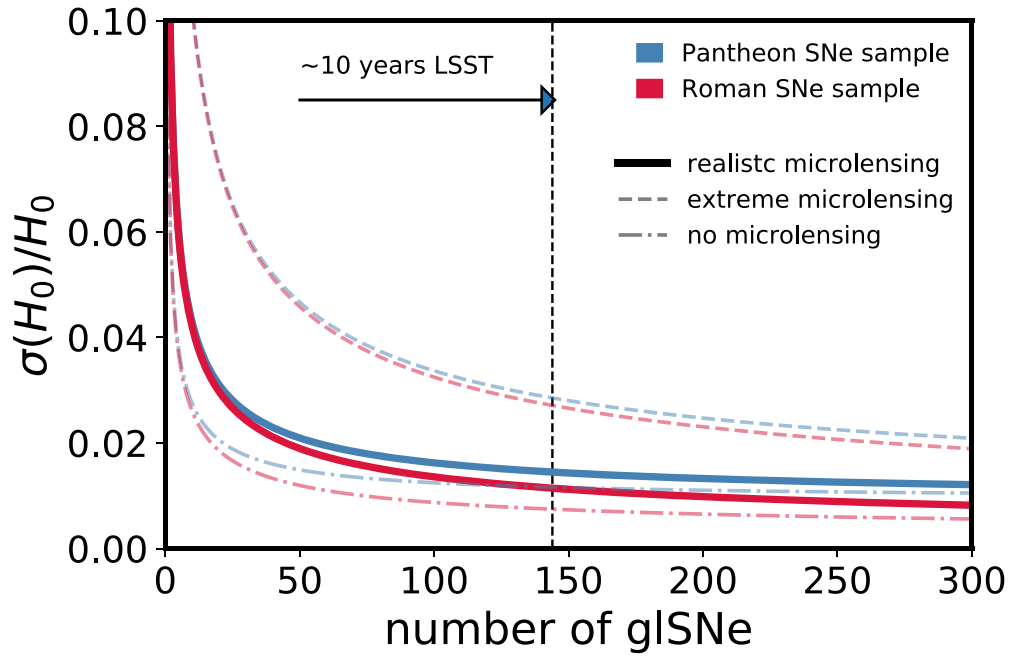
Figure 4. Expected relative precision on H_0 as a function of the number of glSNe with one standardizable image magnification. Blue curves indicate the forecast with the Pantheon SN sample (Scolnic et al. 2018), and red curves indicate the forecast with a future Roman SN sample (Hounsell et al. 2018). Thick solid lines mark our REALISTIC expectations of microlensing (relative uncertainty of $\sigma_{\rm eff,\ std}(m)$ (Equation (51)) of 0.2). Dashed–dotted lines mark the IDEAL scenario of zero microlensing (relative uncertainty of $\sigma_{\rm eff,\ std}(m)$ of 0.0). Dashed lines mark an extreme microlensing scenario (relative uncertainty of $\sigma_{\rm eff,\ std}(m)$ of 1.0). The vertical black dashed line marks the expected number of 144 glSNe for a 10 yr LSST survey, with one image being only marginally affected by microlensing (Goldstein & Nugent 2017; Foxley-Marrable et al. 2018) and an assumed optimal follow-up effort enabling the analysis. The quality and systematic uncertainties in the unlensed field SN sample significantly impact the uncertainty budget for the expected number of glSNe. Calculations are made with the analytical error propagation of Section 3.5. https://github.com/sibirrer/glSNe/Notebooks/analytic_error_propagation.ipnb

magnification effect to break the MST, it is crucial to understand and reproduce the relative selection effect to the percent level. A survey and discovery strategy must account for the feasibility to reproduce the selection function it contains. Known selection effects can then be mitigated by, e.g., large-scale simulations (see, e.g., Scolnic & Kessler 2016; Kessler & Scolnic 2017, for the use for field SN samples).

4. *Extension of the hierarchical analysis to incorporate the astrophysics of microlensing.* The microlensing event statistics is by itself a phenomenon that can probe the compact matter composition and fraction (e.g., Schechter & Wambsganss 2002; Kochanek 2004). Correlations between stellar surface brightness and (microlensing) magnification events allows one to distinguish and measure the stellar initial mass function and other forms of compact objects, such as primordial black holes.

6. Conclusions

Strongly lensed SNe (glSNe) can provide, in addition to measurable time delays, lensing magnification constraints when knowledge about the unlensed apparent brightness of the explosion is imposed. In this paper, we discussed the theoretical aspects that allow absolute lensing magnifications to constrain a key property of the lensing mass profile that is insufficiently constrained with lensing-only data owing to the MSD. We then presented a hierarchical Bayesian analysis framework to combine a data set of SNe that are not strongly lensed and a data set of strongly lensed SNe with measured relative time delays. We jointly constrain (i) the unlensed apparent magnitude distribution of the population of SNe, (ii)

the lens model profiles with the magnification ratio of lensed and unlensed fluxes on the population level, (iii) the relative expansion history of the universe with the relative brightness of SNe with redshift, and (iv) H_0 with the time delays as an absolute distance indicator.

We applied our joint inference framework on a future expected data set of glSNe from 10 yr of the Rubin Observatory LSST in combination with a future unlensed SN sample from the Roman Space Telescope. We forecast that a sample of 144 glSNe with well-measured time series and imaging data have the statistical power to measure H_0 to 1.0% in the next decade.

We discuss further expected covariant systematic uncertainties due to relative selection effects, dust extinction, and SN redshift evolution. We discussed strategies to mitigate systematics associated with using absolute flux measurements of glSNe to constrain the mass density profiles. Among the key systematic effect are relative selection biases in the discovery and usage of the glSNe and the unlensed SN population due to microlensing magnification effects. We emphasize that for a 1% precision on H_0, a 2% overall accuracy in the standardization of apparent brightness distributions between the SN population in the field and the glSN population needs to be achieved. With an additional 1% systematic uncertainty we forecast an overall precision on H_0 of 1.5%.

The methodology presented in this work is implemented in the public software HIERARC and compatible with the hierarchical analysis by Birrer et al. (2020). The implementation allows one to combine different observational constraints self-consistently and can be adopted to the uncertain predictions of the expected glSNe depending on survey and follow-up strategies.
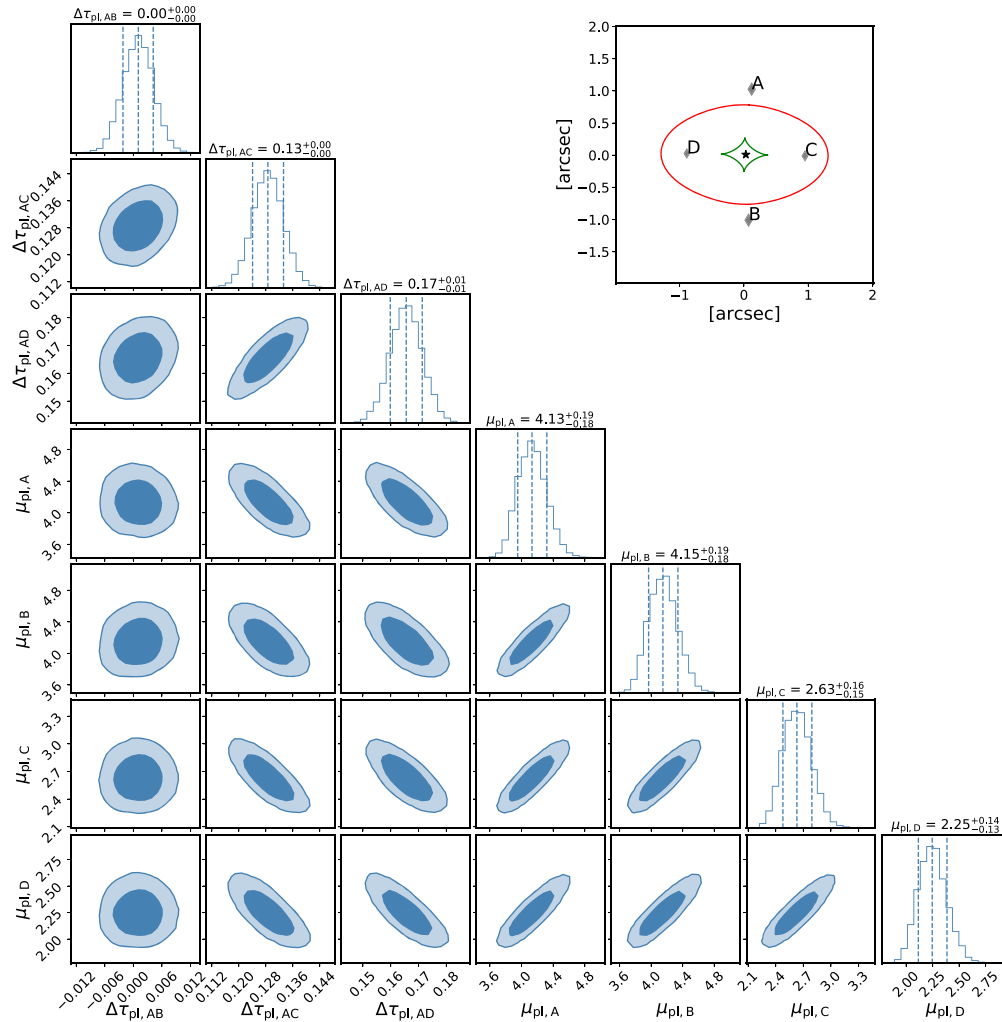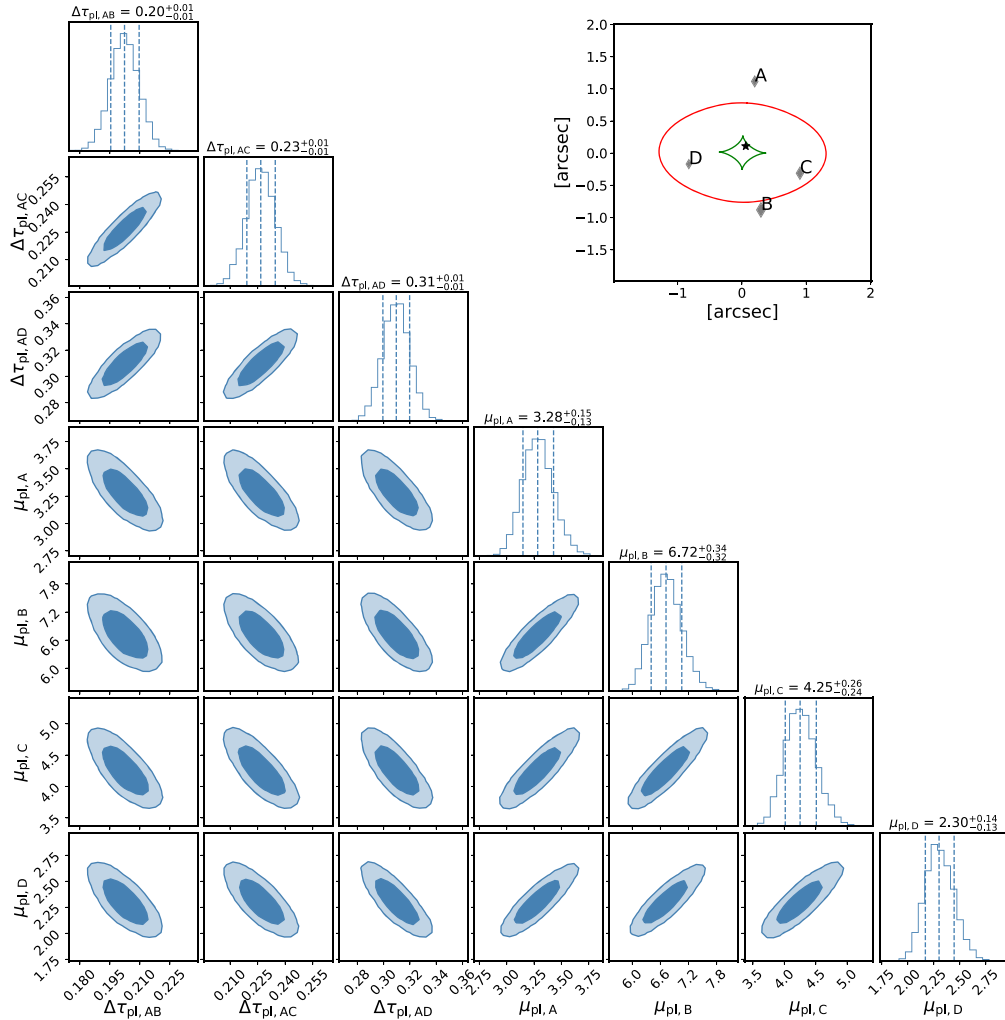
Figure 5. Mock image modeling posterior on the relative Fermat potential and lensing magnification between the image positions of a glSN when fit by a PEMD +shear lens model for the cross configuration. The lens model parameters and uncertainties are presented in Table 3. The configuration of the image position (diamonds), inner caustic (green), and critical curve (red) is illustrated in the top right panel.

Using SNe is a promising and complementary alternative to using stellar kinematics observations to constrain the radial mass density profiles of strong-lensing deflectors and can achieve comparable precision to independent assumptions and systematics. Future surveys, such as the Rubin and Roman observatories, will be able to discover the necessary number of glSNe, and with dedicated additional follow-up observations this methodology will provide precise constraints on mass density profiles and H_0. These constraints will be key to understanding the source of the current Hubble tension and will additionally provide insights into the formation and evolution of massive elliptical galaxies.

Data Availability

The formalism and inference schemes presented in this work are implemented in HIERARC,[17] and the scripts to reproduce the presented work are publicly available.[18] Lensing calculations are performed with LENSTRONOMY.[19]

Lens Model Posteriors

In this appendix, we provide the posteriors of the Fermat potential differences and lensing magnification for the three quad and three double lensing configuration based on the lens model and source position parameters and uncertainties of Table 3. We present the quadruply lensed configurations of the cross in Figure 5 and the fold configuration in Figure 6. The cusp configuration is presented in the main body of the text in Figure 1. The posteriors for the three double configurations are provided in Figure 7.

---

[17] https://github.com/sibirrer/hierArc
[18] https://github.com/sibirrer/glSNe
[19] https://github.com/sibirrer/lenstronomy

Figure 6. Mock image modeling posterior on the relative Fermat potential and lensing magnification between the image positions of a glSN when fit by a PEMD +shear lens model for the fold configuration. The lens model parameters and uncertainties are presented in Table 3. The configuration of the image position (diamonds), inner caustic (green), and critical curve (red) is illustrated in the top right panel.
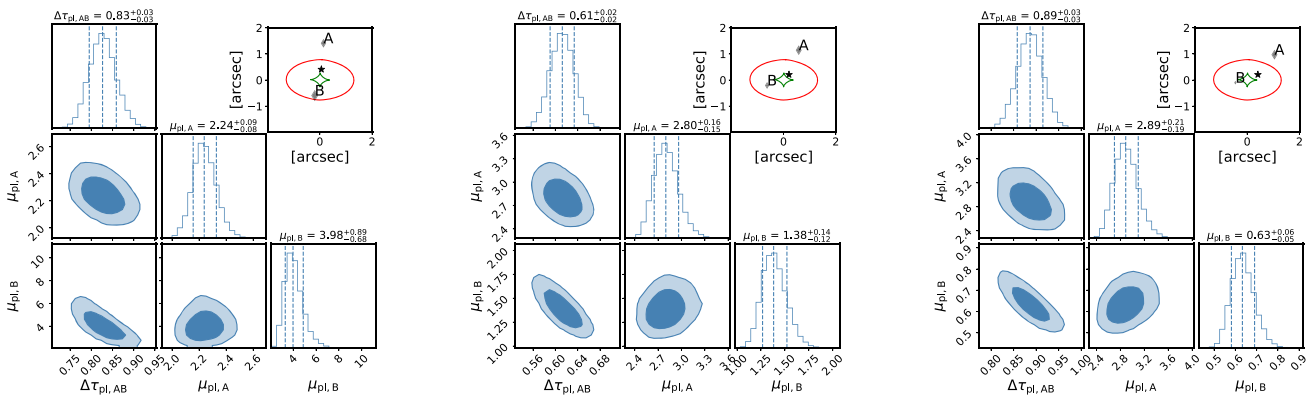

Figure 7. Mock image modeling posterior on the relative Fermat potential and lensing magnification between the image positions of a glSN when fit by a PEMD +shear lens model for the double #1 (left), #2 (middle), and #3 (right) configuration. The lens model parameters and uncertainties are presented in Table 3. The configuration of the image position (diamonds), inner caustic (green), and critical curve (red) is illustrated in the top right panel.

ORCID iDs

Simon Birrer ⓘ https://orcid.org/0000-0003-3195-5507
Suhail Dhawan ⓘ https://orcid.org/0000-0002-2376-6979
Anowar J. Shajib ⓘ https://orcid.org/0000-0002-5558-888X

References

Abbott, T. M. C., Allam, S., Andersen, P., et al. 2019, ApJL, 872, L30
Aiola, S., Calabrese, E., Maurin, L., et al. 2020, JCAP, 2020, 047
Astropy Collaboration, Price-Whelan, A. M., Sipőcz, B. M., et al. 2018, AJ, 156, 123

Astropy Collaboration, Robitaille, T. P., Tollerud, E. J., et al. 2013, A&A, 558, A33
Auger, M. W., Treu, T., Bolton, A. S., et al. 2010, ApJ, 724, 511
Bagherpour, H., Branch, D., & Kantowski, R. 2006, ApJ, 638, 946
Barkana, R. 1998, ApJ, 502, 531
Barnabè, M., Czoske, O., Koopmans, L. V. E., Treu, T., & Bolton, A. S. 2011, MNRAS, 415, 2215
Bayer, J., Huber, S., Vogl, C., et al. 2021, A&A, 653, A29
Betoule, M., Kessler, R., Guy, J., et al. 2014, A&A, 568, A22
Binney, J., & Mamon, G. A. 1982, MNRAS, 200, 361
Birrer, S. 2021, ApJ, 919, 38
Birrer, S., & Amara, A. 2018, PDU, 22, 189
Birrer, S., Amara, A., & Refregier, A. 2015, ApJ, 813, 102
Birrer, S., Amara, A., & Refregier, A. 2016, JCAP, 2016, 020
Birrer, S., Shajib, A. J., Galan, A., et al. 2020, A&A, 643, A165
Birrer, S., Shajib, A. J., Gilman, D., et al. 2021, JOSS, 6, 3283
Birrer, S., & Treu, T. 2019, MNRAS, 489, 2097
Birrer, S., & Treu, T. 2021, A&A, 649, A61
Birrer, S., Treu, T., Rusu, C. E., et al. 2019, MNRAS, 484, 4726
Birrer, S., Welschen, C., Amara, A., & Refregier, A. 2017, JCAP, 2017, 049
Blandford, R., & Narayan, R. 1986, ApJ, 310, 568
Blum, K., Castorina, E., & Simonović, M. 2020, ApJL, 892, L27
Bolton, A. S., Burles, S., Koopmans, L. V. E., et al. 2008, ApJ, 682, 964
Brout, D., & Scolnic, D. 2021, ApJ, 909, 26
Cappellari, M. 2008, MNRAS, 390, 71
Chen, G. C. F., Fassnacht, C. D., Suyu, S. H., et al. 2019, MNRAS, 490, 1743
Coupon, J., Broadhurst, T., & Umetsu, K. 2013, ApJ, 772, 65
Courbin, F., Bonvin, V., Buckley-Geer, E., et al. 2018, A&A, 609, A71
Dalal, N., & Kochanek, C. S. 2002, ApJ, 572, 25
de Jaeger, T., González-Gaitán, S., Anderson, J. P., et al. 2015, ApJ, 815, 121
Dejonghe, H., & Merritt, D. 1992, ApJ, 391, 531
Dhawan, S., Johansson, J., Goobar, A., et al. 2020, MNRAS, 491, 2639
Ding, X., Liao, K., Birrer, S., et al. 2021, MNRAS, 504, 5621
Dobler, G., & Keeton, C. R. 2006, ApJ, 653, 1391
Efstathiou, G. 2020, arXiv:2007.10716
Falco, E. E., Gorenstein, M. V., & Shapiro, I. I. 1985, ApJ, 289, L1
Fassnacht, C. D., Xanthopoulos, E., Koopmans, L. V. E., & Rusin, D. 2002, ApJ, 581, 823
Fleury, P., Larena, J., & Uzan, J.-P. 2021a, CQGra, 38, 085002
Fleury, P., Larena, J., & Uzan, J.-P. 2021b, JCAP, 2021, 024
Foreman-Mackey, D., Hogg, D. W., Lang, D., & Goodman, J. 2013, PASP, 125, 306
Foxley-Marrable, M., Collett, T. E., Vernardos, G., Goldstein, D. A., & Bacon, D. 2018, MNRAS, 478, 5081
Freedman, W. L. 2021, ApJ, 919, 16
Freedman, W. L., Madore, B. F., Hatt, D., et al. 2019, ApJ, 882, 34
Freedman, W. L., Madore, B. F., Hoyt, T., et al. 2020, ApJ, 891, 57
Gilman, D., Agnello, A., Treu, T., Keeton, C. R., & Nierenberg, A. M. 2017, MNRAS, 467, 3970
Gilman, D., Birrer, S., Nierenberg, A., et al. 2020a, MNRAS, 491, 6077
Gilman, D., Birrer, S., & Treu, T. 2020b, A&A, 642, A194
Gilman, D., Birrer, S., Treu, T., Nierenberg, A., & Benson, A. 2019, MNRAS, 487, 5721
Goldstein, D. A., & Nugent, P. E. 2017, ApJL, 834, L5
Goldstein, D. A., Nugent, P. E., & Goobar, A. 2019, ApJS, 243, 6
Goldstein, D. A., Nugent, P. E., Kasen, D. N., & Collett, T. E. 2018, ApJ, 855, 22
Goobar, A., Amanullah, R., Kulkarni, S. R., et al. 2017, Sci, 356, 291
Goobar, A., Mörtsell, E., Amanullah, R., & Nugent, P. 2002, A&A, 393, 25
Greene, J. E., Murphy, J. D., Graves, G. J., et al. 2013, ApJ, 776, 64
Guy, J., Astier, P., Baumont, S., et al. 2007, A&A, 466, 11
Guy, J., Sullivan, M., Conley, A., et al. 2010, A&A, 523, A7
Hounsell, R., Scolnic, D., Foley, R. J., et al. 2018, ApJ, 867, 23
Hsueh, J. W., Enzi, W., Vegetti, S., et al. 2020, MNRAS, 492, 3047
Hsueh, J. W., Fassnacht, C. D., Vegetti, S., et al. 2016, MNRAS, 463, L51
Huber, S., Suyu, S. H., Noebauer, U. M., et al. 2019, A&A, 631, A161
Huber, S., Suyu, S. H., Noebauer, U. M., et al. 2021, A&A, 646, A110
Johansson, J., Goobar, A., Price, S. H., et al. 2021, MNRAS, 502, 510
Keeton, C. R., & Moustakas, L. A. 2009, ApJ, 699, 1720

Kelly, P. L., Rodney, S. A., Treu, T., et al. 2015, Sci, 347, 1123
Kessler, R., & Scolnic, D. 2017, ApJ, 836, 56
Kochanek, C. S. 2002, ApJ, 578, 25
Kochanek, C. S. 2004, ApJ, 605, 58
Kochanek, C. S. 2020, MNRAS, 493, 1725
Kochanek, C. S. 2021, MNRAS, 501, 5021
Kolatt, T. S., & Bartelmann, M. 1998, MNRAS, 296, 763
Kundić, T., Turner, E. L., Colley, W. N., et al. 1997, ApJ, 482, 75
Liao, K., Ding, X., Biesiada, M., Fan, X.-L., & Zhu, Z.-H. 2018, ApJ, 867, 69
McCully, C., Keeton, C. R., Wong, K. C., & Zabludoff, A. I. 2014, MNRAS, 443, 3631
McCully, C., Keeton, C. R., Wong, K. C., & Zabludoff, A. I. 2017, ApJ, 836, 141
Miller, A. A., Yao, Y., Bulla, M., et al. 2020, ApJ, 902, 47
Millon, M., Courbin, F., Bonvin, V., et al. 2020a, A&A, 640, A105
Millon, M., Galan, A., Courbin, F., et al. 2020b, A&A, 639, A101
More, A., Suyu, S. H., Oguri, M., More, S., & Lee, C.-H. 2017, ApJL, 835, L25
Mortsell, E., Goobar, A., Johansson, J., & Dhawan, S. 2021, arXiv:2105.11461
Nugent, P., Sullivan, M., Ellis, R., et al. 2006, ApJ, 645, 841
Oguri, M. 2019, RPPh, 82, 126901
Oguri, M., & Kawano, Y. 2003, MNRAS, 338, L25
Oguri, M., & Marshall, P. J. 2010, MNRAS, 405, 2579
Park, J. W., Wagner-Carena, S., Birrer, S., et al. 2021, ApJ, 910, 39
Petrushevska, T., Amanullah, R., Bulla, M., et al. 2017, A&A, 603, A136
Phillips, M. M. 1993, ApJL, 413, L105
Pierel, J. D. R., Rodney, S., Vernardos, G., et al. 2021, ApJ, 908, 190
Planck Collaboration, Aghanim, N., Akrami, Y., et al. 2020, A&A, 641, A6
Poznanski, D., Nugent, P. E., & Filippenko, A. V. 2010, ApJ, 721, 956
Refsdal, S. 1964, MNRAS, 128, 307
Riess, A. G., Casertano, S., Yuan, W., et al. 2021, ApJL, 908, L6
Riess, A. G., Casertano, S., Yuan, W., Macri, L. M., & Scolnic, D. 2019, ApJ, 876, 85
Rigault, M., Aldering, G., Kowalski, M., et al. 2015, ApJ, 802, 20
Rodney, S. A., Patel, B., Scolnic, D., et al. 2015, ApJ, 811, 70
Rusu, C. E., Fassnacht, C. D., Sluse, D., et al. 2017, MNRAS, 467, 4220
Rusu, C. E., Wong, K. C., Bonvin, V., et al. 2020, MNRAS, 498, 1440
Schechter, P. L., Bailyn, C. D., Barr, R., et al. 1997, ApJL, 475, L85
Schechter, P. L., & Wambsganss, J. 2002, ApJ, 580, 685
Schneider, P. 1985, A&A, 143, 413
Schneider, P., Ehlers, J., & Falco, E. E. 1992, Gravitational Lenses, Astronomy and Astrophysics Library (Berlin: Springer)
Schneider, P., & Sluse, D. 2013, A&A, 559, A37
Scolnic, D., & Kessler, R. 2016, ApJL, 822, L35
Scolnic, D. M., Jones, D. O., Rest, A., et al. 2018, ApJ, 859, 101
Shajib, A. J., Birrer, S., Treu, T., et al. 2020, MNRAS, 494, 6072
Shajib, A. J., Treu, T., Birrer, S., & Sonnenfeld, A. 2021, MNRAS, 503, 2380
Sonnenfeld, A. 2018, MNRAS, 474, 4648
Suyu, S. H., Auger, M. W., Hilbert, S., et al. 2013, ApJ, 766, 70
Suyu, S. H., Huber, S., Cañameras, R., et al. 2020, A&A, 644, A162
Suyu, S. H., Marshall, P. J., Auger, M. W., et al. 2010, ApJ, 711, 201
Suyu, S. H., Marshall, P. J., Blandford, R. D., et al. 2009, ApJ, 691, 277
Taubenberger, S. 2017, in The Extremes of Thermonuclear Supernovae, ed. A. W. Alsabti & P. Murdin (Cham: Springer), 317
Tessore, N., & Metcalf, R. B. 2015, A&A, 580, A79
Tewes, M., Courbin, F., Meylan, G., et al. 2013, A&A, 556, A22
Thorp, S., Mandel, K. S., Jones, D. O., Ward, S. M., & Narayan, G. 2021, MNRAS, 508, 4310
Tihhonova, O., Courbin, F., Harvey, D., et al. 2018, MNRAS, 477, 5657
Treu, T., & Koopmans, L. V. E. 2002, ApJ, 575, 87
Wagner-Carena, S., Park, J. W., Birrer, S., et al. 2021, ApJ, 909, 187
Weisenbach, L., Schechter, P., & Pontula, S. 2021, ApJ, 922, 70
Wojtak, R., Hjorth, J., & Gall, C. 2019, MNRAS, 487, 3342
Wong, K. C., Suyu, S. H., Auger, M. W., et al. 2017, MNRAS, 465, 4895
Wong, K. C., Suyu, S. H., Chen, G. C. F., et al. 2020, MNRAS, 498, 1420
Yahalomi, D. A., Schechter, P. L., & Wambsganss, J. 2017, arXiv:1711.07919
Yao, Y., Miller, A. A., Kulkarni, S. R., et al. 2019, ApJ, 886, 152
Yıldırım, A., Suyu, S. H., & Halkola, A. 2020, MNRAS, 493, 4783